Mitochondrial Hyperactivity and Reactive Oxygen Species Drive Innate Immunity to the Yellow Fever Virus-17D Live-Attenuated Vaccine

Samantha G. Muccilli[1,2], Benjamin Schwarz[3], Forrest Jessop[4], Jeffrey G. Shannon[1], Eric Bohrnsen[3], Byron Shue[1], Seon-Hui Hong[5], Thomas Hsu[1], Alison W. Ashbrook[5], Joseph W. Guarnieri[6], Justin Lack[7], Douglas C. Wallace[6], Catharine M. Bosio[4], Margaret R. MacDonald[5], Charles M. Rice[5], Jonathan W. Yewdell[2], Sonja M. Best[1]*

[1]Innate Immunity and Pathogenesis Section, Laboratory of Neurological Infections and Immunity, Rocky Mountain Laboratories, NIAID, NIH, Hamilton, MT; [2]Cellular Biology Section, Laboratory of Viral Diseases, NIAID, NIH, Bethesda, MD; [3]Research Technologies Branch, NIAID, NIH, Hamilton, MT; [4]Immunity to Pulmonary Pathogens Section, Laboratory of Bacteriology, NIAID, NIH, Hamilton, MT; [5]Laboratory of Virology and Infectious Disease, The Rockefeller University, New York, NY; [6]Center for Mitochondrial and Epigenomic Medicine, Children's Hospital of Philadelphia, Philadelphia, PA; [7]Integrated Data Sciences Section, Research Technologies Branch, NIAID, NIH

**Corresponding author: sbest@niaid.nih.gov*

Summary

The yellow fever virus 17D (YFV-17D) live attenuated vaccine is considered one of the successful vaccines ever generated associated with high antiviral immunity, yet the signaling mechanisms that drive the response in infected cells are not understood. Here, we provide a molecular understanding of how metabolic stress and innate immune responses are linked to drive type I IFN

expression in response to YFV-17D infection. Comparison of YFV-17D replication with its parental virus, YFV-Asibi, and a related dengue virus revealed that IFN expression requires RIG-I-like Receptor signaling through MAVS, as expected. However, YFV-17D uniquely induces mitochondrial respiration and major metabolic perturbations, including hyperactivation of electron transport to fuel ATP synthase. Mitochondrial hyperactivity generates reactive oxygen species (mROS) and peroxynitrite, blocking of which abrogated IFN expression in non-immune cells without reducing YFV-17D replication. Scavenging ROS in YFV-17D-infected human dendritic cells increased cell viability yet globally prevented expression of IFN signaling pathways. Thus, adaptation of YFV-17D for high growth uniquely imparts mitochondrial hyperactivity generating mROS and peroxynitrite as the critical messengers that convert a blunted IFN response into maximal activation of innate immunity essential for vaccine effectiveness.

Keywords: Yellow fever virus, live-attenuated vaccine, mitochondria, electron transport, reactive oxygen species, type I interferon

Introduction

Yellow fever virus (YFV) is the prototypical *Orthoflavivirus*, positive-stranded RNA arboviruses that cause significant global morbidity and mortality each year [1]. Between the 15th and 19th centuries, yellow fever was among the most devastating infectious diseases in old and new worlds, including a 1793 outbreak that killed approximately 10% of Philadelphia's population in the USA [2-4]. Walter Reed discovered YFV as the etiological agent early in the 20th century. In rapid succession the *Aedes aegypti* mosquito was identified as its vector and the YFV-17D strain was

47 generated as one of the most effective vaccines of all time [5-7]. Despite this, YFV remains an
48 important human pathogen, causing approximately 80,000-200,000 infections annually with an
49 estimated 40% mortality rate, mainly in Central and South America and Africa [8].
50
51 The YFV-17D vaccine was empirically derived by serial passage of a virulent YFV strain (YFV-
52 Asibi) in mouse and chicken embryos [6, 7]. Administered to more than 500 million people
53 worldwide, YFV-17D elicits strong innate and adaptive immune responses, and confers lifelong
54 immunity to yellow fever in more than 95% of vaccinees [9]. YFV-17D robustly induces cytotoxic
55 T cells, T_H1 and T_H2 CD4 T cells, and neutralizing antibodies that persist for 40 or more years [10,
56 11]. The strength and quality of the adaptive immune response is strongly influenced by detectable
57 viremia [12] and a robust innate immune signature [13-15]. All three classes of interferons (IFNs)
58 are linked to inducing and shaping the adaptive immune response to the virus, as well as controlling
59 YFV-17D replication and dissemination *in vivo* [16-18]. While the vaccine is considered safe, a
60 small number of vaccinees (1/250,000) develop yellow fever vaccine-associated viscerotropic
61 disease or neurotropic disease [8, 19]. Patients with compromised type I IFN function are at a
62 higher risk of developing disseminating infection [20, 21]. Therefore, the innate immune response
63 is considered the cornerstone of the success of the YFV-17D vaccine in both control of virus
64 replication and induction of adaptive immunity. The extent to which signaling pathways uniquely
65 engaged by YFV-17D drive heightened IFN and inflammatory responses compared to the parental
66 strain or other orthoflaviviruses is central to our study.
67
68 Several different pattern recognition receptors (PRRs) can be activated in response to infection
69 with orthoflaviviruses to initiate an antiviral response. These include RIG-I-like receptors (RLRs),

70 toll-like receptors (TLRs) and the DNA sensing pathway cGAS-STING. Previous work examining
71 IFN responses to YFV-17D used mouse bone marrow-derived dendritic cells (DCs) and suggested
72 that multiple TLRs are engaged to produce IFNs and other pro inflammatory cytokines [18].
73 However, YFV does not productively replicate in mouse cells including monocytes and DCs. This
74 makes mice a poor model for understanding how innate responses are activated given that cytosolic
75 RLRs are essential in initiating innate immune responses that control orthoflavivirus dissemination
76 and tissue tropism, and license downstream adaptive immune responses in IFN-competent models
77 [22].
78
79 RLRs signal through the adaptor protein mitochondrial antiviral signaling protein (MAVS) to
80 induce expression of IFNs, chemokines and pro-inflammatory cytokines. MAVS is localized on
81 mitochondria and peroxisomes, and its oligomerization on mitochondrial membranes is required
82 for assembling the MAVS signalasome to activate IRF3, IRF7 and NFκB transcription factors
83 [23]. Accordingly, viruses manipulate the structure and inter-organellar communication of the
84 mitochondria, peroxisomes, and ER to dampen innate immune signaling and enhance replication.
85 For example, the orthoflavivirus dengue virus (DENV) induces mitochondrial elongation and
86 convoluted membrane formation resulting in reduced ER-mitochondria contact sites and
87 dampened MAVS signaling [24]. Conversely, viral mitochondrial manipulation to meet the
88 metabolic needs of viral replication and dampen MAVS-dependent signaling can result in the
89 release of mitochondrial DNA sensed by cGAS-STING that activates the IFN response [25-27].
90
91 In addition to PRR signaling, metabolic dysregulation and cellular stress responses may contribute
92 to immune responses to YFV-17D vaccination. In humans, symptomatic responses to YFV-17D

93 vaccination correlated with ER stress, reduced tricarboxylic acid (TCA) cycle functionality,
94 increased plasma levels of reactive oxygen species (ROS), and induction of cellular redox genes
95 [28]. Furthermore, the magnitude of adaptive immune responses to vaccination can be predicted
96 by gene expression involved in glycolysis and the integrated stress response [9, 29]. Together,
97 these findings indicate a role for metabolic stress in activating the immune response to YFV-17D
98 vaccination. However, mechanisms of metabolic stress and how they integrate with pathogen
99 sensing and innate immunity in the context of YFV-17D replication are not known. Here, we
100 provide a molecular understanding of the linkage between metabolic stress and innate immune
101 responses to the YFV-17D vaccine that underpin its resounding success.
102
103
104 **Results**
105
106 *Hepatotropic orthoflaviviruses induce distinct type I interferon dynamics independently of*
107 *mitochondrial morphology.*
108 To understand the contribution of mitochondrial dynamics to YFV-17D activation of innate
109 immune responses, we first compared multi-cycle virus growth kinetics and type I IFN expression
110 between YFV-17D, YFV-Asibi, and DENV2 in HepG2 and Huh7 human hepatoma cell lines
111 (Figure 1A, Supplemental Figure 1A). While the viruses attained similar peak titers in HepG2
112 cells, YFV-17D reached near peak titer in the first 24 hours, while YFV-Asibi and DENV2
113 required an additional 24 h. IFNβ was detected in YFV-17D-infected cell supernatants by 48 hpi,
114 increasing for another day. Peak expression was at least 10-fold higher than present in YFV-Asibi
115 or DENV2-infected cell supernatants, as previously reported [30]. Of note, Huh7 cells failed to

116 secrete measurable IFNβ following YFV-17D or DENV2 infection despite being highly
117 permissible to infection (Supplemental Figure 1A). Based on the robust IFN response, HepG2 cells
118 were selected for further experiments. siRNA targeting critical adaptor proteins, MAVS and
119 STING, was used to characterize the dominant pathway of IFNβ induction. Depletion of MAVS
120 resulted in a near complete reduction of IFNβ secretion following infection with YFV-17D (Figure
121 1B) or DENV2 (Figure 1C). In contrast, reduced STING expression did not affect IFNβ following
122 YFV-17D infection, but reduced IFNβ production late in DENV2 infection, consistent with
123 existing literature that mitochondrial DNA release late in DENV infection is sensed by
124 cGAS/STING to contribute to induction of type I IFN [31]. These results confirm RLR-dependent
125 signaling is a dominant mechanism of orthoflavivirus sensing in non-immune cells.
126
127 As orthoflaviviruses manipulate the structure and function of mitochondria, the predominant
128 location of MAVS, we next examined the effects of viral infection on mitochondrial morphology
129 via immunofluorescence staining for the outer membrane protein TOM20 and the viral
130 nonstructural protein NS3 (Figure 1D). In mock-infected cells, mitochondria formed branched
131 networks of intermediate length. As previously reported, DENV2 infection induced elongation and
132 tangling of the mitochondrial network [24]. Conversely, infection with either YFV-17D or YFV-
133 Asibi resulted in loss of branched mitochondrial networks in favor of individual, swollen
134 mitochondria. Quantification of mitochondrial shape confirmed that YFV infection induced
135 mitochondrial rounding at both 24hpi and 48hpi (Figure 1E). We extended these findings to Huh7
136 cells; DENV2 infection also induced mitochondrial elongation while YFV caused significant
137 mitochondrial rounding and swelling (Supplemental Figure 1B).
138

139 Alterations in mitochondrial shape have a major impact on mitochondrial and cellular physiology.
140 Mitochondrial elongation facilitates MAVS oligomerization and IFNβ production, while fission
141 hinders MAVS' ability to form high-order oligomers and impairs signaling [32, 33]. We next
142 explored how manipulating mitochondrial networks modulates flavivirus induction of IFNβ using
143 siRNA to deplete mitochondrial GTPases. Dynamin-related protein 1 (DRP1) has a major role in
144 mitochondrial fission, while mitofusin 2 (MFN2) mediates mitochondrial fusion. As expected,
145 DRP1 depletion elongated mitochondria while MFN2 depletion fragmented mitochondria in
146 uninfected cells (Figure 2A). However, in YFV-17D infected cells fragmentation of mitochondria
147 occurred under conditions of DRP1 depletion, suggesting that viral infection supersedes DRP1
148 dependence for mitochondrial fission. By contrast, mitochondrial hyperfusion in DENV2-infected
149 cells was dependent on MFN2, as reported [24]. Virus replication was slightly increased (YFV-
150 17D; Figure 2B) or was not significantly affected (DENV2; Figure 2C) by loss of MFN2 or DRP1.
151 Surprisingly, knockdown of either protein resulted in significant loss of IFNβ production following
152 infection with either virus (Figure 2B-2C). In contrast, in cells infected with Sendai virus (SeV, a
153 paramyxovirus), a canonical inducer of MAVS-dependent IFNβ-expression, IFNβ secretion was
154 increased in DRP1 siRNA-treated cells and decreased in cells depleted for MFN2 as has been
155 previously published (Figure 2D). Together with the high IFNβ response by YFV-17D infected
156 cells that display a fragmented mitochondrial phenotype, these data indicate that MAVS-
157 dependent expression of IFNβ in response to infection with these hepatotropic flaviviruses is
158 divorced from canonical mitochondrial morphology dynamics.
159
160 *YFV-17D drives rapid cellular energetic expenditure.*

161 We next used LC-MS-based metabolomics to determine how flavivirus-induced mitochondrial
162 alterations correlate with metabolic changes in cells at 48 hpi. Principle component analysis (PCA)
163 revealed that YFV-17D infection induced a distinct metabolic phenotype compared to mock, YFV-
164 Asibi, or DENV2-infected cells (Figure 3A). Over 50% of measured metabolites were
165 differentially abundant in YFV-17D infected cells compared to mock-infected cells with an FDR
166 < 10% (Figure 3B). Conversely, YFV-Asibi and DENV2-infected cells had very few changes in
167 metabolic intermediates relative to mock-infected cells despite major alterations in mitochondrial
168 morphology (Figure 3A). Analysis of differentially abundant metabolites revealed that YFV-17D
169 infection starkly depleted high-energy triphosphates in favor of the low energy monophosphates
170 (Figure 3C, D), indicative of either energetic exhaustion or a high rate of energetic expenditure.
171 Triphosphate pools were reduced to a lesser extent in YFV-Asibi or DENV2 infected cells.
172 Metabolomic analysis performed 24 and 36 hpi revealed mock and YFV-17D infected cells were
173 metabolically similar (Figure 3E). At these two timepoints, respectively, only two and five
174 metabolites were differentially abundant between mock- and YFV-17D infected cells while
175 triphosphate ratios were minimally different or unchanged (Figure 3F, Supplemental Figure 3).
176 The tri/monophosphate ratios together with the lack of major metabolic changes indicate that this
177 significant metabolic expenditure does not commence until after 36 hpi. Together, these data
178 indicate that YFV-17D infection leads to rapid and intense metabolic expenditure that coincides
179 with IFNβ secretion.
180
181 *YFV-17D infection drives mitochondrial hyper-functionality and energetic overcommitment.*
182 We next used seahorse extracellular flux analysis to measure oxygen consumption over time in the
183 presence of electron transport chain inhibitors to isolate the effects of infection on mitochondrial

184 function. First, basal respiration is measured, then ATP-synthase is blocked by oligomycin to
185 calculate the proportion of oxygen used for ATP synthesis. Next, the proton gradient is collapsed
186 by FCCP that allows electrons to flow unimpeded across the inner mitochondrial membrane to
187 measure maximal respiration rate. Spare respiratory capacity, a measurement of the cell's ability
188 to respond to an increase in energetic demands during metabolic stress, can be calculated by
189 subtracting the maximal respiration rate from the basal respiration rate. Finally, a combination of
190 complex I inhibitor rotenone and complex III inhibitor Antimycin A entirely abolish mitochondrial
191 respiration, enabling calculation of non-mitochondrial respiration (Figure 4A-4B)[34].
192
193 Significantly increased basal respiration was evident as early as 12 hpi with YFV-17D. Notably,
194 by 48hpi, the basal respiration rate of YFV-17D infected cells was nearly equal to the maximal
195 respiration rate. ATP-linked respiration is the primary contributor to this basal respiratory
196 elevation in the YFV-17D infected cells as represented by the difference between basal respiration
197 and respiration following oligomycin addition. Further, YFV-17D infected cells increased the rate
198 of glycolysis between 24 and 48 hpi as measured by metabolomics and Seahorse assays
199 (Supplemental Figure 4A-C). Thus, YFV-17D infection maximizes mitochondrial respiration even
200 under basal conditions, resulting in a significant decrease in mitochondrial spare respiratory
201 capacity. In contrast, mitochondrial function was not changed by DENV2 infection, except for a
202 decrease in basal respiration and glycolysis observed at 48 hpi.
203
204 In general, high mitochondrial respiration is associated with increased oxidative phosphorylation
205 and ATP production. Yet, the metabolomics analysis indicated that YFV-17D infection depletes
206 ATP. Therefore, we sought to verify the metabolomics by quantifying total ATP concentration in

207 infected cells. Indeed, despite substantial increases in total- and ATP synthase-linked respiration
208 at 48 hpi, YFV-17D infected cells had a significantly lower standing pool of ATP compared to
209 DENV2- or mock-infected cells (Figure 4C). The concomitant increases in glycolysis and ATP
210 synthase-linked respiration, drop in spare respiratory capacity, maintenance of maximal
211 respiration, and drop in triphosphate pools suggest extremely high energetic demands in the YFV-
212 17D infected cells that is outpacing the maximally available triphosphate synthesis.
213
214 While the seahorse analysis suggested increased mitochondrial function and health, the
215 discordance of the flux data with ATP levels suggested that additional stressors and processes may
216 be present in the mitochondria that were invisible to the measure of respiration under controlled
217 conditions. To assess mitochondrial function in situ, we next measured mitochondrial membrane
218 potential using flow cytometry. Mitochondrial membrane potential is driven by the electron
219 transport chain pumping protons into the intermembrane space that are then used by ATP synthase
220 to produce ATP. In a healthy cell, at equilibrium, the electron transport chain pumps more protons
221 than ATP synthase consumes resulting in a high mitochondrial membrane potential. Interestingly,
222 we found mitochondrial membrane potential decreased precipitously in YFV-17D infected cells
223 beginning at 32hpi, while DENV2-infected cells maintained mitochondrial membrane potential
224 (Figure 4D). This low mitochondrial membrane potential in conjunction with high ATP synthase-
225 linked respiration indicates the mitochondrial depolarization is likely caused by ATP-synthase
226 outpacing the ability of the electron transport chain to replenish the proton pool. This disconnect
227 between electron transport and ATP synthesis is unsustainable and places the cell under significant
228 metabolic stress. Together these data indicate that YFV-17D infection requires enormous amounts
229 of ATP to keep up with the metabolic demands of infection. The cell makes every attempt to meet

230 this extreme metabolic burden including upregulating both glycolysis and mitochondrial
231 respiration. Thus, mitochondria become hyper-functional and energetically overcommitted,
232 upregulating ATP synthase activity to the point that ATP synthesis surpasses the rate of
233 mitochondrial respiration. While minimal cell death was apparent at the time of these
234 measurements up to 48 hpi, the cell is eventually no longer able to maintain the rapid rate of
235 mitochondrial respiration and ATP synthesis and succumbs to cell death by 72 hpi as measured by
236 Annexin V staining (Supplemental Figure 5).
237
238 To alleviate concern that the major phenotypes that differentiate YFV-17D infection from its
239 parental strain are a result of mutations acquired during tissue culture passage of the viruses, we
240 repeated select assays using molecular viral clones. Recombinant YFV-17D and YFV-Asibi
241 derived from molecular clones mirrored the tissue culture passaged lab stocks in growth kinetics,
242 IFNβ secretion, and differential loss of mitochondrial membrane potential (Supplemental Figure
243 6A-C). Notably, although a dose-dependent effect of MOI was apparent for induction of IFNβ
244 secretion and mitochondrial membrane potential loss during YFV-17D infection, increasing
245 infection burden by YFV-Asibi did not increase IFNβ secretion or induce loss of mitochondrial
246 membrane potential by 48 hpi (Supplemental Figure 6C). Thus, these phenotypes represent virus-
247 encoded differences between YFV-17D and YFV-Asibi.
248
249 *YFV-17D-induced ROS is responsible for activating type I interferon signaling.*
250 In addition to the generation of ATP, mitochondrial respiration also generates mitochondrial
251 reactive oxygen species (mROS) that can activate a pro-inflammatory state in cells [35, 36]. YFV-
252 17D induced mROS over baseline levels measured by Mitosox labeling by 24 hpi whereas for

253 DENV2, increased mROS required an additional 24 hours (Figure 5A-B). Treating cells with the
254 cell permeable ROS scavenger MnTBAP at either 0 or 24 hpi did not impede replication of YFV-
255 17D or DENV2. However, IFNβ production in YFV-17D infected cultures was reduced
256 approximately 10-fold to levels equivalent to those produced following DENV2 infection (Figure
257 5C-D). MnTBAP treatment only delayed the induction of IFNβ by DENV2-infeccted cells.
258 Importantly, this finding demonstrates that high levels of IFNβ secretion are separable from virus
259 replication and accompanying high levels of viral molecular patterns and reveals that mROS is a
260 critical factor required to drive high levels of IFNβ by YFV-17D.
261
262 Given that the type I IFN response is incredibly energy intensive and that MAVS activation results
263 in mitochondrial depolarization, we sought to determine if mitochondrial hyperactivity and
264 energetic overcommitment was driven by a need to supply ATP for innate immune signaling or if
265 this mitochondrial phenotype precedes IFN production. However, inhibition of IFNβ production
266 using either MnTBAP or siRNA to deplete cells of MAVS did not rescue the loss of mitochondrial
267 membrane potential following YFV-17D infection (Supplemental Figure 7). Thus, mitochondrial
268 overcommitment is driven directly by YFV-17D replication rather than the cell-intrinsic, energy
269 intensive process of type I IFN signaling.
270
271 MnTBAP also scavenges peroxynitrite, a ROS species generated from superoxide and nitric oxide
272 [37]. Peroxynitrite induction closely mirrored that of IFNβ induction during YFV-17D replication
273 (Supplemental Figure 8A), and MnTBAP significantly decreased cellular peroxynitrite
274 (Supplemental Figure 8B). Inhibiting nitric oxide synthase with L-NAME (Supplemental Figure
275 8C) also significantly decreased IFNβ expression following infection, consistent with peroxynitrite

276 being a major contributor to IFNβ secretion (Supplemental Figure 8E). Finally, since high levels
277 of ROS are cytotoxic, we investigated the effect of MnTBAP on cell viability. Treatment with
278 MnTBAP partially rescued YFV-17D infected cells from death, consistent with linkage of type I
279 IFN induction and cell death via ROS generation (Figure 5F). Taken together, our data indicate
280 that YFV-17D uniquely induces maximal mitochondrial respiration that is unable to keep up with
281 the metabolic needs of the cell. This metabolic stress results in enhanced mROS and peroxynitrite
282 generation which greatly amplifies MAVS-dependent IFN signaling while also mediating cell
283 death.
284
285 *ROS is required for human dendritic cells to mount an innate antiviral response to YFV-17D*
286 *infection*
287 Dendritic cells (DCs) are professional antigen presenting cells that are both important targets of
288 YFV infection and required for activation of naïve T cells. Given their critical role in vaccination
289 of naïve individuals, we examined the role of ROS in virus-induced DC activation. Monocyte-
290 derived DCs from five human donors were infected with YFV-17D in the presence of MnTBAP
291 or vehicle control. While viral replication rates varied among donors (Figure 6A), IFNβ was
292 detected in all infected cultures by 48 hpi (Figure 6B). As with HepG2 infection, MnTBAP
293 treatment significantly decreased IFNβ expression and increased cell viability in all five donors
294 without affecting viral replication (Figure 6C, A).
295
296 Global gene expression changes were assessed in DCs by bulk RNA sequencing at 48 hpi. Pathway
297 enrichment analysis revealed that YFV-17D infection significantly upregulated mRNA involved
298 in the innate immune response and cell death and downregulated protein translation associated

299 mRNA (Figure 6D). MnTBAP treatment downregulated IFN signaling in infected cells (Figure
300 6E), with six of the top twenty downregulated pathways related to IFN signaling. Notably, multiple
301 type I and III IFNs as well as interferon stimulated genes demonstrated ROS dependence
302 (Supplemental Table 1). Global IFN signaling downregulation was accompanied by
303 downregulating of genes involved in chemokine signaling (data not shown), pointing to a broad
304 role for ROS signaling in chemotaxis and DC based T cell help.
305
306 Consistent with a central role for oxidative stress responses in cell-intrinsic responses to infection,
307 key antioxidant enzymes (GSR, CAT, GPX1, and PRDX1) were downregulated by YFV-17D
308 (Supplemental Figure 9A) and select genes (SOD2, NFE2L2, and KEAP1) were upregulated by
309 MnTBAP treatment. Thus, YFV-17D infection likely increases oxidative stress by inducing
310 mitochondrial ROS in concert with reducing cellular antioxidant capabilities. Together, our
311 findings demonstrate that expression of type I and III IFNs and chemokines, considered hallmarks
312 of YFV-17D vaccine responses, depend on a virus-induced metabolic program culminating in high
313 ROS generation coincident with initiation of RLR signaling. ROS is therefore the critical
314 secondary messenger that converts relatively low-level PRR signaling into the extraordinary
315 induction of innate immunity following YFV-17D infection.
316
317
318 **Discussion**
319
320 Compared to other licensed vaccines, including live-attenuated viruses and recombinant viral
321 vectors, the YFV-17D vaccine induces unique immune signatures in human vaccinees associated

322 with detectable viremia and delayed but robust innate responses [38]. The magnitude of
323 neutralizing antibody and cytotoxic T cell responses correlate with the viremic load and antiviral
324 cytokine and chemokine responses [12, 39]. In addition, cellular metabolic and stress responses
325 enhance MHC I and II restricted antigen presentation and correlate with CD8 T cell responses [40,
326 41]. YFV-17D vaccine gene signatures have been predominantly ascribed to TLR stimulation [9,
327 18]. However, the dominant pattern recognition pathway controlling orthoflavivirus replication in
328 IFN-competent animal models is MAVS-dependent [22]. Orthoflaviviruses also manipulate
329 mitochondrial quality control pathways to facilitate replication and evade RLR signaling,
330 amplifying the integrated stress and inflammatory responses [24, 42]. These fundamental features
331 of orthoflavivirus infection and innate immune activation prompted us to reexamine the
332 contribution of MAVS-dependent signaling and mitochondrial function to YFV-17D triggering of
333 innate immunity as measured by IFNβ secretion.
334
335 As shown previously, YFV-17D replicates rapidly when compared to its parental strain YFV-Asibi
336 or DENV2 [30]. Rapid replication is associated with major metabolic and mitochondrial
337 perturbations. YFV-17D infection maximizes mitochondrial respiration to a rate that is
338 energetically unsustainable. Indeed, our data indicate that YFV-17D infection causes ATP-
339 synthase to consume protons faster than they can be supplied by the electron transport chain
340 resulting in a rapid progressive reduction in mitochondrial membrane potential. Notably, this
341 mitochondrial hyperactivity is independent of type I IFN signaling indicating that this is a process
342 virally encoded rather than a side effect of an overactive innate immune response. Despite an
343 extraordinary rate of ATP production as measured by highly elevated ATP-linked respiration, cells
344 are still unable to meet the energetic demands of infection resulting in depletion of standing ATP

345 pools. The onset of this metabolic stress is coincident with ROS generation and RLR activation.
346 Thus, the metabolic stress of YFV-17D infection drives a reprioritization of nutrient/energetic
347 resources to ROS generation and cytokine production prior to cell death. Importantly, blocking
348 ROS-based signaling did not reduce viral replication. Thus even in the presence of high levels of
349 viral molecular patterns, ROS is the key factor that translates relatively low RLR pathway
350 activation into the YFV-17D hallmark innate immune signature. In human DCs, ROS signaling
351 was critical for expression of type I and III IFNs, a spectrum of chemokines, ISGs, and cell death
352 pathway activation, all which likely contribute to an adaptive immune response that confers
353 lifelong protection from yellow fever. Importantly, this study reveals the cell biology of infection
354 contributing to gene signatures associated with symptomatic responses and correlated with
355 magnitude of adaptive immunity in humans following YFV-17D vaccination [9,13-15, 29].
356
357 Mitochondrial fusion, fission, and mitophagy are essential for maintaining cellular function.
358 Viruses manipulate mitochondria to enhance replication through provision of metabolic
359 intermediates for RNA replication as well as suppression of innate immune responses and
360 apoptosis [43-45]. During RLR signaling, MAVS activation is aided by an intact mitochondrial
361 membrane potential, and increased mitochondria surface area and ER-contacts [33, 44, 46].
362 Indeed, we confirmed important aspects of this model in the context of Sendai virus as a canonical
363 RLR signaling activator. In Sendai virus infected cells, depleting MFN2 fragments mitochondria
364 and reduces IFNβ secretion while depleting DRP1 elongates mitochondria and increases IFNβ
365 secretion. However, while both YFV-Asibi and YFV-17D induced mitochondrial fragmentation,
366 mitochondria in YFV-17D infected cells support high MAVS-dependent IFNβ secretion. We
367 hypothesize that wild type YFV evolved to fragment mitochondria to dampen MAVS signaling to

368 enhance replication and that this property was maintained in generating YFV-17D [47]. However,
369 in the case of YFV-17D, infection-induced metabolic and oxidative stress negates any advantage
370 provided by fragmented mitochondrial morphology. While YFV-induced mitochondrial
371 fragmentation is independent of DRP1 (the major GTPase responsible for fission in uninfected
372 cells), YFV-17D-induced IFNβ required both DRP1 and MFN2. MFN2-dependence is consistent
373 with its role in adapting macrophage mitochondrial respiration to metabolic stress and promoting
374 mROS generation [48]. The requirement for DRP1 in YFV-induced MAVS-dependent signaling
375 is puzzling, particularly as DRP1 is inactivated by TBK1 to facilitate MAVS responses [49],
376 necessitating further work to interpret this finding. Nevertheless, our results indicate that while
377 mitochondrial morphology strongly contributes to MAVS-based anti-viral immunity, other factors
378 can override its canonical role.
379
380 Viral-induced alterations in metabolism favoring glycolysis, as we observed in YFV-17D-infected
381 HepG2 cells, likely evolve in part to increase nucleotide levels via the pentose phosphate pathway
382 to support viral replication [50]. Similar metabolic reprogramming is critical in allowing virus-
383 activated DCs to become optimal antigen-presenting cells. Increased glycolytic flux is required
384 for TBK1-, IKKε- and Akt- dependent DC activation [51]. MAVS signaling is also regulated by
385 glycolysis and activates the same kinases, consistent with these processes being linked in DCs
386 [52]. Immune cell activation is also closely associated with ROS production. Similarly,
387 mitochondrial hijacking by DENV, influenza A, and vesicular stomatitis virus results in ROS
388 generation that enhances RLR and MAVS signaling [53, 54]. We confirmed a requirement for
389 ROS in early expression of IFNβ by DENV-infected cells. While ROS is generally involved in

390 RLR innate immune activation, the timing and magnitude of ROS-dependent IFNβ secretion
391 points to critical differences between YFV-17D and related viruses.
392
393 Although the mechanism linking ROS to MAVS-dependent RLR signaling remains to be
394 elucidated in the context of YFV-17D, several possibilities exist. Activated MAVS forms large,
395 prion-like surface mitochondrial aggregates that are necessary and sufficient to activate
396 downstream type I IFN signaling. It is well established that ROS-based MAVS aggregation
397 generated by virus infection, chemicals, or systemic lupus erythematosus facilitates type I IFN
398 signaling [55]. It is hypothesized that ROS oligomerizes MAVS by oxidizing specific cysteine
399 residues, promoting disulfide bond formation and/or by peroxidizing lipids in the mitochondrial
400 membrane, favoring MAVS transmembrane domain oligomerization [55, 56]. This might explain
401 the critical role of mROS in YFV-17D induced IFNβ secretion, although there may be a
402 contribution from ROS activation of NF-κB, AP-1, MAPK, and PI3K pathways [57]. Additionally,
403 we show that YFV-17D infection induces the specific ROS species peroxynitrite, which via
404 various alterations to proteins, lipids, sugars and nucleotides [58, 59], can independently influence
405 metabolism and immune responses [60-62]. Additional studies are required to precisely define the
406 contribution of ROS-based mechanisms to YFV-17D immune activation in liver cells and DCs.
407
408 Much also remains to be learned about how our findings relate to YFV-17D attenuation. Our data
409 indicate that high metabolic burden is critical in augmenting the innate immune response to YFV-
410 17D relative to YFV-Asibi and DENV2, which may be driven by rapid replication. YFV-17D
411 differs from YFV-Asibi at 68 nucleotide positions, resulting in 32 non-synonymous codon changes
412 scattered throughout the genome. Twelve changes are present in the viral envelope protein [63],

413 conferring increased viral attachment and entry, increasing replication and enhancing
414 proinflammatory pathway activation [30, 64]. This may contribute to our finding that robust YFV-
415 17D replication leads to metabolic stress and mitochondrial overcommitment, culminating in
416 ROS-induced type-I IFN signaling and cell death. In this case, paradoxically, high viral replication
417 would be beneficial to the host as it leads to recognition and control of YFV-17D before significant
418 viral dissemination can occur. Substitutions in non-structural proteins may also contribute to high
419 RNA replication, or directly interfere with mitochondrial function. Indeed, mitochondrial
420 manipulation has been attributed to nonstructural proteins NS4A and NS5 of DENV and ZIKV,
421 respectively [24, 42]. Future reverse genetic-based mapping studies using the molecular clones
422 used herein should elucidate the relevant mutations in YFV-17D responsible for its remarkable
423 vaccine efficacy. This information will be useful for designing not only future flavivirus vaccines,
424 but likely vaccines for a wide variety of viruses.
425

426 **Acknowledgements:**
427 This work was supported by the Division of Intramural Research, National Institutes of Health,
428 National Institute of Allergy and Infectious Diseases, and R01AI124690 to CMR.
429

430 **Declaration of Interests**
431 The authors declare no competing interests.
432

433 **Experimental Procedures**
434 *Cell Culture*

435 We cultured HepG2 cells (ATCC) and Vero E76 cells (ECACC) in DMEM (Gibco) supplemented
436 with 10% FBS (Cytiva) and 1% penicillin/streptomycin (Gibco) at 37˚C and 5% CO_2. We cultured
437 C636 mosquito cells (ATCC) in MEM (Gibco) supplemented with 10% heat-inactivated FBS,
438 2mM Glutamine (Gibco), 1% NEAA (Gibco), and 1% penicillin/streptomycin at 32˚C and 5%
439 CO_2.
440
441 *Virus Infections*
442 We used the following viruses in this study: yellow fever virus (YFV) strain 17D (from NIH
443 Biodefense and Emerging Infections Research Recourses Repository, NIAID, NIH, NR116); YFV
444 strain Asibi (from University of Texas Medical Branch World Reference Center for Emerging
445 Viruses and Arboviruses); dengue virus (DENV) strain New Guinea C (from Dr. Adolfo García-
446 Sastre); Sendai virus (SeV) strain Cantell (from Charles River Laboratories). We performed all
447 procedures with YFV-Asibi under biosafety level-3 (BSL-3) conditions at the Rocky Mountain
448 Laboratories Integrated Research Facility (Hamilton, MT). We propagated orthoflavivirus
449 working stocks on C636 cells and titrated by plaque assay on Vero cells. Multiplicity of infection
450 (MOI) is represented as plaque forming units (PFU) per cell. For all experiments, we infected cells
451 for 1 hour at 37˚C before removing virus inoculum and replacing with fresh culture medium.
452
453 *Immunofluorescence*
454 We coated 4 well Lab-Tek II chamber coverglass slides (Thermo Fisher Scientific) with poly-l-
455 lysine for 1 hour at 37˚C prior to seeding cells. Following the culture period, we washed and fixed
456 cells for 15 minutes at 37˚C in 4% paraformaldehyde (Electron Microscopy Sciences) diluted in
457 DMEM. Following fixation, we washed cells several times and permeabilized with 0.1% Triton

458 X-100/sodium citrate (Sigma Aldrich) for 15 minutes at room temperature before washing several
459 more times. We blocked in 3% normal goat serum for 1 hour and then incubated overnight at 4˚C
460 in primary antibody diluted in 1% normal goat serum (Abcam). We washed cells and incubated
461 with secondary antibody diluted in 1% normal goat serum for 1 hour at room temperature followed
462 by Hoescht (Thermo Fisher Scientific) for 5 minutes at room temperature. We washed and stored
463 cells at 4˚C until imaging. We imaged processed slides using either a Zeiss LSM710 confocal
464 microscope or a Leica Stellaris 8 confocal microscope and analyzed images using the FIJI
465 software.
466
467 *Western Blot*
468 We washed and lysed cells in SDS extraction buffer (50 mM Tris pH 7.4, 150 mM sodium chloride,
469 1mM EDTA, 2% SDS) supplemented with complete protease inhibitor (Sigma Aldrich). Lysates
470 were agitated at 95˚C for 10 minutes. We quantified protein concentration using the DC Protein
471 assay (Bio-Rad) per the manufacturer's protocol before diluting lysates 1:4 in sample buffer (90%
472 4X Protein Loading Buffer (LiCor), 10% DTT (Sigma Aldrich)). We heated diluted samples at
473 70˚C for 10 minutes. We resolved 12 µg of cell lysate on 4-12% Bis-Tris gels (Thermo Fisher
474 Scientific) and transferred to Nitrocellulose or PVDF membranes (Invitrogen) using the iBlot 2
475 Transfer System (Invitrogen). We blocked the membrane for 1 hour with Intercept Blocking Buffer
476 (LiCor) followed by overnight incubation at 4˚C in primary antibody diluted in blocking buffer.
477 We washed membranes three times for 5 minutes with PBST before incubating at room
478 temperature for 1 hour in secondary antibody diluted in blocking buffer. We washed membranes
479 several times with PBST before imaging on the LiCor Odyssey CLx Imager.
480

481 *siRNA Treatment*

482 We used the following siRNAs: Horizon ON-TARGETplus SMARTpool siRNAs specific against
483 DRP1 (L-012092), MAVS (L-024237), MFN2 (L-012961), and STING (L-024333). We
484 transfected HepG2 cells with 20 mmol siRNA using the Lipofectamine RNAiMAX reagent (Life
485 Technologies) according to the manufacturer's protocol. We incubated cells with siRNA proceed
486 for 48 hours prior to infection and downstream analysis.

487

488 *Metabolite Sample Preparation*

489 We washed HepG2 cells with a 0.9% sodium chloride solution at room temperature. To quench
490 cellular metabolism, we added ice-cold LCMS-grade methanol (Fisher Chemical) and incubated
491 on ice for 5 minutes. We added an equal volume of ice-cold LCMS-grade water (Fisher Chemical)
492 before scraping cells and transferring samples to polypropylene tubes which were stored at -80˚C
493 until analysis. We randomized samples across plates to account for minor variations in sample
494 collection time. The aqueous fraction was taken for LCMS analysis and diluted as needed in a 1:1
495 mixture of methanol and water to balance signal intensity.

496

497 *Liquid Chromatography Mass Spectrometry*

498 We purchased tributylamine and all synthetic molecular references from Millipore Sigma. We
499 purchased LCMS grade water, methanol, isopropanol and acetic acid through Fisher Scientific.
500 We analyzed aqueous metabolites using a combination of two analytical methods with opposing
501 ionization polarities [65, 66]. Both methodologies utilized a LD40 XR UHPLC (Shimadzu Co.)
502 system for separation. Negative mode samples were separated on a Waters™ Atlantis T3 column
503 (100Å, 3 µm, 3 mm X 100 mm) and eluted using a binary gradient from 5 mM tributylamine, 5

504 mM acetic acid in 2% isopropanol, 5% methanol, 93% water (v/v) to 100% isopropanol over 5
505 minutes. Signals were detected using a 5500 QTrap mass spectrometer (AB Sciex Pte. Ltd.). Two
506 distinct MRM pairs in negative mode were used for each metabolite. Positive mode method
507 samples were separated across a Phenomenex Kinetex F5 column (100 Å, 2.6 µm, 100 x 2.1 mm)
508 and eluted with a gradient from 0.1% formic acid in water to 0.1% formic acid in acetonitrile over
509 5 minutes. Signals were detected using a 6500+ QTrap mass spectrometer (AB Sciex Pte. Ltd.).
510 All signals were integrated using SciexOS 3.1 (AB Sciex Pte. Ltd.). Signals with greater than 50%
511 missing values for a specific tissue set were discarded and remaining missing values were replaced
512 with the lowest registered signal value. Where appropriate, signals with a QC coefficient of
513 variance greater than 30% were discarded. Metabolites with multiple MRMs were quantified with
514 the higher signal to noise MRM. The filtered dataset of the negative mode aqueous metabolites
515 was total sum normalized after initial filtering. The positive mode aqueous metabolomics dataset
516 was scaled and combined with the negative mode aqueous metabolite dataset using a common
517 signal for serine. A Benjamini-Hochberg method for correction for multiple comparisons was
518 imposed where indicated.
519
520 *Seahorse Extracellular Flux Analysis*
521 We seeded Hep2G cells at 1×10^4 cells per well in a XFe96 tissue culture plate (Agilent
522 Technologies) and incubated for 24 hours in cDMEM. We infected cells with mock, YFV-17D
523 (MOI 0.1) or DENV2 (MOI 1) as previously described. At 12-, 24-, and 48-hours post infection
524 we performed extracellular flux analysis to interrogate the impacts of infection on mitochondrial
525 function and glycolysis Prior to extracellular flux analyses, we washed cells twice with 200 µL
526 of assay medium (minimal DMEM with 25 mM glucose, 2 mM sodium pyruvate, and 2 mM L-

527 glutamine (Agilent Technologies)). We incubated cells in 180 µL Assay medium for 1 hour at
528 37˚C in a non-CO_2 incubator. We measured oxygen consumption rate (OCR) rate at baseline and
529 following injection of oligomycin A1 (2 µM, MilliporeSigma), fluoro-carbonyl cyanide
530 phenylhydrazone (FCCP; 2 µM; Cayman Chemical), and rotenone/antimycin (0.5 µM final
531 concentration for both; MilliporeSigma). We used corresponding extracellular acidification rates
532 (ECAR) as surrogate markers of changes in glycolytic flux. We performed all extracellular flux
533 assays on the Seahorse XFe96 Analyzer (Agilent Technologies).
534
535 *Flow Cytometry*
536 We used the following cellular dyes: TMRE (Abcam), MitoSOX (Abcam), Peroxynitrite Green
537 (Abcam), and Annexin V/PI (Thermo Fisher Scientific) according to the respective manufacturer's
538 protocol. Following staining, we washed cells several times with PBS and split into single cell
539 solution using trypsin. When appropriate, we also stained cells with the Live/Dead Fixable Aqua
540 Dead Cell Stain (Thermo Fisher Scientific) for 20 minutes on ice to identify the live cell
541 population. Flow cytometry analysis was performed on a BD LSR Fortessa X-20 flow cytometer.
542
543 *ATP Quantitation*
544 We extracted ATP from cells using the boiling water method to minimize ATPase depletion. We
545 washed HepG2 cells twice with PBS and then added boiling highly purified water (ThermoFisher),
546 triturating to lyse cells and boiling for several more minutes to completely inactivate ATPases. We
547 stored samples at -80˚C until analysis. We measured in ATP in each sample in triplicate using an
548 ATP Determination Kit (Thermo Fisher Scientific) according to the manufacturer's protocol,
549 analyzing all samples in one assay to maximize reproducibility.

550

551 *Small Molecule Inhibitors*

552 We used MnTBAP (Sigma Aldrich) and L-NAME (Selleck Chemicals). We prepared a 50 mM
553 stock solution of MnTBAP in DMSO (ATCC). Immediately before use, we prepared a reduced
554 working solution by diluting the MnTBAP to a final concentration of 1mM in PBS/4% NaOH
555 [2.5M] (Sigma Aldrich). We added 100µM of the reduced working solution to cells in a drop-wise
556 fashion to minimize cell death. For this treatment, the vehicle control consisted of an equal volume
557 of DMSO in PBS/4% NaOH [2.5M]. Alternately, we treated cells with 5mM L-NAME in sterile
558 water and an equal volume of water was used as a vehicle control for these experiments. For both
559 inhibitors, we retreated cells every 24 hours to maintain high inhibitor concentration.

560

561 *Full-length molecular clones*

562 Full length YFV Asibi virulent strain (MT093734.1) and 17D vaccine strain (MT114401.1)
563 infectious clones have been previously described [67, 68] and are designated pACNR-2015FLYF-
564 Asibi and pACNR-2015FLYF-17Da respectively. The E.coli strain MC1061 was used to amplify
565 these clones. After amplification and purification, plasmid DNA was linearized using AflII,
566 followed by clean up and in vitro transcription using the mMESSAGE mMACHINE SP6
567 transcription kit. The virus stock was produced in Huh7.5 cells using 10µg of RNA essentially as
568 described [69]. Cells of the electroporation reaction were seeded in a T-175 flask. At 4-6 hours
569 post-electroporation, the media was changed and at 20-24 hours post-electroporation, media was
570 replaced with serum free DMEM. Virus stocks were obtained by harvesting the media after an
571 additional 6-8 hours and aliquots were stored at -80°C.

572

573 *Human monocyte-derived dendritic cells*

574 Human monocyte-derived dendritic cells were prepared as previously described [70]. Briefly, we
575 isolated peripheral blood mononuclear cells from human buffy coats (BioIVT) by centrifugation
576 through a Ficoll-Paque Plus density gradient (Cytiva). Cells were enriched for $CD14^+$ monocytes
577 using a RossetteSep Monocyte Enrichment Kit (StemCell Technologies). Monocytes were
578 resuspended at $1x10^6$ cells/mL in DC medium [RPMI + Glutamax (Invitrogen), 5% FBS, 15 mM
579 Hepes, 0.1 mM nonessential amino acids, 1 mM sodium pyruvate, 100 units/mL penicillin and 100
580 μg/mL streptomycin] containing IL-4 (20 ng/mL) and GM-CSF (20 ng/ml) (PeproTech) and
581 cultured for 5d with replacement of half of the medium and addition of fresh cytokines every other
582 day. Nonadherent DC were harvested by centrifugation and suspended in DC medium. The
583 resulting cells were determined to be >95% $CD11c^+$/$CD209^+$ by flow cytometry.

584

585 *Bulk RNA-seq of human DCs*

586 We plated human monocyte-derived DCs at $2x10^6$ cells/well and mock-infected or infected with
587 YFV-17D at an MOI of 0.1 in a small volume for 1 hour at 37˚C, 5% CO_2 with occasional gentle
588 rocking. We added fresh DC medium to the wells to the desired volume and MnTBAP (50 μM)
589 or vehicle control was added to the appropriate wells at 0 and 24 h post-infection. At 48 hpi, we
590 harvested hDCs by centrifugation, and lysed the cells with 1 mL of TRIzol reagent/sample
591 (Thermo Fisher Scientific), and samples were stored at -80˚C before extraction and bulk RNA-
592 seq. We collected cell supernatants at 0 and 48 hpi for cytokine and viral plaque assays.

593

594 For RNA extraction, we mixed the samples with 200 μL of 1-bromo-3-chloropropane (Sigma
595 Aldrich) and centrifuged at 4˚C for 15 minutes at 16,000 x g. We removed the aqueous phase and

596 passed it through a QIAshredder column (Qiagen) at 21,000 x g for 2 minutes. RNA was extracted
597 using the Qiagen AllPrep DNA/RNA system. An additional on-column DNase I treatment was
598 performed for all extractions. We assessed RNA quality using the Agilent 2100 Bioanalyzer RNA
599 6000 Pico kit (Agilent Technologies) and quantified the RNA using the Quant-it RiboGreen RNA
600 assay (Thermo Fisher Scientific).
601
602 Following RNA extraction, two hundred nanograms of RNA was used as the input for the Illumina
603 stranded mRNA prep, ligation kit (Illumina) to generate sequencing libraries following the
604 manufacturer's protocol. The final libraries were analyzed using the Agilent bioanalyzer and the
605 libraries were quantified using the Kapa SYBR FAST Universal qPCR kit for Illumina sequencing
606 (Kapa Biosystems). The individual libraries were diluted to 6 nM and 2 uL of each added to a
607 library pool. The library pool was denatured and diluted to a 10 pM stock and paired-end 2 x 75
608 cycle sequencing carried out on the MiSeq using a Nano V2 flow cell and 300 cycle chemistry.
609 Following the sequencing run, reads per microliter mapping to human genes were determined for
610 each library. The library pool was rebalanced and quantified using the Kapa SYBR FAST
611 Universal qPCR kit for Illumina sequencing. The library pool was diluted to 9 pM and paired-end
612 2 x 75 cycle sequencing carried out on the MiSeq using a Nano V2 flow cell and 300 cycle
613 chemistry. The final library pool containing 6 nM of each library was sent to the National Cancer
614 Institute, Center for Cancer Research Sequencing Facility (NCI CCR-SF) for further sequencing.
615 The samples were paired-end 2 x 100 cycle sequenced using a NovaSeq 6000 instrument and SP
616 flow cell and 300 cycle chemistry.
617

618 Following sequencing, Raw fastq files were trimmed to remove adapters and low-quality bases
619 using Cutadapt v1.18 before alignment to the GRCh38 reference genome and the Gencode v42
620 genome annotation using STAR v2.7.9a [71]. PCR duplicates were marked using the
621 MarkDuplicates tool from the Picard v3.1.0 (https://broadinstitute.github.io/picard/) software
622 suite. Raw gene counts were generated using RSEM v1.3.3 [72] and were filtered to include genes
623 with >=1 count per million (CPM) in at least 2 samples.
624
625 Differential expression was evaluated using limma with TMM normalization [73]. For all
626 differential expression comparisons, pre-ranked geneset enrichment analysis (GSEA) [74] was
627 performed using the Reactome [75] and MitoCarta v3.0 [76].
628
629 *Statistical Analysis*
630 All graphical values are shown as mean ± standard deviation. We performed statistical analyses
631 using GraphPad Prism 10. Ordinary one-way or two-way ANOVAs with Dunnett's multiple
632 comparisons tests were performed, when appropriate, to test statistical significance between
633 means. We considered p-values less that 0.05 to be statistically significant.
634
635
636 **Figure Legends**
637
638 *Figure 1: Dengue virus and yellow fever viruses modulate host mitochondrial and interferon*
639 *dynamics differently.*

640 **A** Growth curve quantifying the viral titer and ELISA quantification of IFNβ secreted by HepG2
641 cells infected with YFV-17D (MOI 0.1), YFV-Asibi (MOI 0.1), or DENV2 (MOI 1) over a 72
642 hour period. **B and C** Growth curve quantifying the viral titer and ELISA quantification of IFNβ
643 secreted by HepG2 cells infected with **B** YFV-17D or **C** DENV2 and treated with siRNAs to
644 knockdown MAVS, STING, or a non-targeting control. **D** Immunofluorescence (IF) of
645 mitochondrial morphology following infection with mock, DENV2 (MOI 1), YFV-17D (MOI
646 0.1), or YFV-Asibi (MOI 1) for 48 hours. Nuclei are stained with DAPI in blue, mitochondria are
647 stained with TOM20 in green, and infected cells are stained with NS3 in red. **E** Quantification of
648 the form factor of the mitochondrial network in HepG2 cells infected with mock, YFV-17D, or
649 YFV-Asibi. Form factor was calculated using the following equation: Form Factor = $(\text{Perimeter})^2$
650 / 4π * Area. Values represent the mean ± SD (n=3). Statistical significance was assessed using
651 two-way ANOVA followed by Tukey's post hoc test for multiple groups (B and C) or ordinary
652 one-way ANOVA followed by Tukey's post hoc test for multiple groups (E). ****$p<0.0001$.
653
654 *Figure 2: The type-I IFN response to YFV-17D and DENV2 is dissociated from mitochondrial*
655 *morphology.*
656 **A** IF of mitochondrial morphology of HepG2 cells following infection with mock, YFV-17D (MOI
657 0.1), or DENV2 (MOI 1) and treated with siRNAs to knockdown DRP1 or MFN2. Nuclei are
658 stained with DAPI in blue, mitochondria are stained with TOM20 in green, and infected cells are
659 stained with NS3 in red. **B and C** Growth curve quantifying the viral titer and ELISA
660 quantification of IFNβ secreted by HepG2 cells infected with **B** YFV-17D or **C** DENV2 and
661 treated with siRNAs to knockdown MFN2, DRP1, or a non-targeting control. **D** ELISA
662 quantification of IFNβ secreted by HepG2 cells infected with Sendai virus and treated with

663 sirRNAs to knockdown MFN2, DRP1, or a non-targeting control. Values represent the mean ± SD
664 (n=3). Statistical significance was assessed using two-way ANOVA followed by Tukey's post hoc
665 test for multiple groups (B-D). *** $p<0.001$ **** $p<0.0001$.
666
667 *Figure 3: YFV-17D drives rapid cellular energetic expenditure.*
668 **A** Principle component analysis (PCA) of metabolomic differences between HepG2 cells infected
669 with mock, DENV2 (MOI 1), YFV-17D (MOI 0.1), or YFV-Asibi (MOI 1) at 48hpi. **B** Volcano
670 plots showing the significantly differentially abundant metabolites between YFV-17D infected
671 HepG2 cells and mock-infected HepG2 cells at 48hpi as defined by metabolites with $p<0.1$
672 equivalent to an FDR of 10% via a Benjamini Hochberg. Metabolites with a fold change of ≥2 or
673 ≤-2 are colored and named. **C** Metabolomic heatmap comparing the abundance of monophosphates
674 and triphosphates following infection with mock, YFV-17D, YFV-Asibi, or DENV2. **D**
675 Quantification of the triphosphate to monophosphate ratios in HepG2 cells infected with mock,
676 YFV-17D, YFV-Asibi, and DENV2 at 48hpi. **E** PCA of metabolomic differences between mock
677 and YFV-17D infected HepG2 cells at 24hpi, 36hpi, and 48hpi. **F** Quantification of the
678 triphosphate to monophosphate ratios in mock and YFV-17D infected HepG2 cells at 24hpi and
679 48hpi. Values represent the mean ± SD (n=6). Statistical significance was assessed using ordinary
680 one-way ANOVA followed by Dunnett's multiple comparisons test (D) or two-way ANOVA
681 followed by Sidak's multiple comparisons test (F). **** $p<0.0001$.
682
683 *Figure 4: YFV-17D induces mitochondrial hyper-functionality and energetic overcommitment.*
684 **A** Seahorse XF cell mito stress test profile of HepG2 cells infected with mock, YFV-17D (MOI
685 0.1), or DENV2 (MOI 1) at 12hpi, 24hpi, and 48hpi. **B** Quantification of several Seahorse XF mito

686 stress test parameters (basal respiration, maximal respiration, ATP-linked respiration, and spare
687 respiratory capacity) in mock, YFV-17D, or DENV2 infected HepG2 cells over a 48 hour period.
688 **C** Quantification of intracellular ATP levels in mock, YFV-17D, and DENV2 infected HepG2
689 cells at 24hpi and 48hpi. **D** Quantification of mitochondrial membrane potential (TMRE) in mock,
690 YFV-17D, and DENV2 infected HepG2 cells between 24hpi and 72hpi. Values represent the mean
691 ± SD (B: n=12, C: n=4, D: n=3). Statistical significance was assessed using two-way ANOVA
692 followed by Dunnett's multiple comparisons test (B, C, D). * $p<0.05$, ** $p<0.01$, *** $p<0.001$,
693 **** $p<0.0001$.
694
695 *Figure 5: YFV-17D-induced ROS is responsible for activating the type-I IFN response and cell*
696 *death during YFV-17D infection.*
697 **A** IF of mitochondrial ROS production using MitoSOX dye in HepG2 cells infected with mock,
698 YFV-17D (MOI 0.1), or DENV2 (MOI 1) at 24hpi, 48hpi, and 72hpi. **B** Quantification of
699 MitoSOX staining in mock, YFV-17D, and DENV2 infected HepG2 cells using flow cytometry.
700 **C and D** Growth curve quantifying the viral titer and ELISA quantification of IFNβ secreted by
701 HepG2 cells infected with **C** YFV-17D or **D** DENV2 and treated with MnTBAP [100μM] at 0hpi
702 or 24hpi. **E** Flow cytometric quantification of MitoSOX staining in mock, YFV-17D, and DENV2
703 infected HepG2 cells treated with MnTBAP or a vehicle control for 48 hours. **F** Flow cytometric
704 quantification of viability of mock, YFV-17D, and DENV2 infected HepG2 cells treated with
705 MnTBAP or a vehicle control for 48 hours. Values represent the mean ± SD (B, C, D, F: n=3; E:
706 n=2). Statistical significance was assessed using two-way ANOVA followed by Tukey's post hoc
707 test for multiple groups (B-D) or ordinary one-way ANOVA followed by Tukey's post hoc test
708 for multiple groups (E, F). * $p<0.05$, ** $p<0.01$, *** $p<0.001$, **** $p<0.0001$.

709

710

711 *Figure 6: mROS is required for primary human dendritic cells to properly mount an innate immune*

712 *response to YFV-17D infection*

713 **A** Growth curve quantifying the viral titer of human DCs from five donors infected with YFV-

714 17D (MOI 0.1) over a 48 hour period. **B** ELISA quantification of IFNβ secreted by DCs infected

715 with either mock or YFV-17D. **C** Pathway enrichment analysis of YFV-17D infected DCs

716 compared to mock infected DCs at 48hpi. **D** Pathway enrichment analysis of YFV-17D infected

717 DCs treated with MnTBAP compared to vehicle control at 48hpi. Values represent the mean ± SD

718 (n=2). Statistical significance was assessed using ordinary one-way ANOVA followed by Sidak's

719 multiple comparisons test (B). **** $p<0.0001$.

720

721

722 *Supplemental Figure 1: Differential mitochondrial morphodynamics are consistent across*

723 *multiple cell types*

724 **A** Growth curve quantifying the viral titer and ELISA quantification of IFNβ secreted by Huh7

725 cells infected with YFV-17D (MOI 0.1) or DENV2 (MOI 0.1) over a 72 hour period. **B** IF of

726 mitochondrial morphology in Huh7 cells following infection with mock, DENV2 (MOI 1), YFV-

727 17D (MOI 0.1), or YFV-Asibi (MOI 1) for 48 hours. Nuclei are stained with DAPI in blue,

728 mitochondria are stained with TOM20 in green, and infected cells are stained with NS3 in red.

729

730 *Supplemental Figure 2: siRNA treatment results in knockdown of host proteins*

731 Western blot quantifying protein following siRNA treatment with **A** siMAVS, **B** siSTING, **C**
732 siMFN2, and **D** siDRP1. Treatment with siRNA resulted in significant knockdown of the
733 respective protein.
734
735 *Supplemental Figure 3: Very few metabolites are differentially abundant between YFV-17D and*
736 *mock infected cells at 24 and 36 hpi.*
737 **A and B** Volcano plots showing the significantly differentially abundant metabolites between
738 YFV-17D infected Hep G2 cells and mock-infected HepG2 cells at **A** 24hpi and **B** 36hpi.
739
740 *Supplemental Figure 4: YFV-17D upregulates glycolysis between 24 and 48 hpi.*
741 **A** Metabolomic heatmap comparing the abundance of metabolites from the glycolytic pathway,
742 pentose-5-phosphate pathway, and nucleotides following infection with mock, YFV-17D (MOI
743 0,1), YFV-Asibi (MOI 1), or DENV2 (MOI 1) in HepG2 cells. **B** Schematic of the glycolysis
744 pathway with metabolites significantly downregulated in YFV-17D infection at 48hpi shown in
745 blue and metabolites significantly upregulated in YFV-17D infection at 48hpi shown in red. **C**
746 Schematic of the glycolysis and pentose-5-phosphate pathway with metabolites significantly
747 downregulated in YFV-17D infection at 48hpi shown in in blue and metabolites significantly
748 upregulated in YFV-17D infection at 48hpi shown in red. **D** Quantification of the media
749 acidification rate obtained during the Seahorse XF mito stress test in mock, YFV-17D, or DENV2
750 infected HepG2 cells over a 48 hour period. Values represent the mean ± SD (n=12). Statistical
751 significance was assessed using two-way ANOVA followed by Dunnett's multiple comparisons
752 test (D). * $p<0.05$, ** $p<0.01$, *** $p<0.001$, **** $p<0.0001$.
753

754

755 *Supplemental Figure 5: YFV-17D does not induce apoptosis until late timepoints.*

756 **A** Representative flow cytometry dot plots quantifying Annexin V and propidium iodide in mock,
757 YFV-17D (MOI 0.1), and DENV2 (MOI 1) infected HepG2 cells at 24hpi, 48hpi, and 72hpi. **B**
758 Quantification of the percentage of apoptotic cells in mock, YFV-17D, and DENV2 infected cells
759 at 24hpi, 48hpi, and 72hpi. Values represent the mean ± SD (n=3). Statistical significance was
760 assessed using two-way ANOVA followed by Dunnett's multiple comparisons test (D). ****
761 $p<0.0001$.

762

763 *Supplemental Figure 6: Infectious clones mirror the phenotypes of lab stock viruses*

764 **A** Growth curve quantifying viral titer of HepG2 cells infected with YFV-17D (MOI 0.1) or YFV-
765 Asibi (MOI 0.1) generated from lab stocks or infectious clones over a 48 hour period. **B** ELISA
766 quantification of IFNβ secreted by HepG2 cells infected with lab stocks or infectious clones at 24
767 and 48 hpi. **C** Quantification of mitochondrial membrane potential (TMRE) in HepG2 cells
768 infected with lab stock or infectious clone viruses at 48hpi. Values represent the mean ± SD (A,
769 B: n=3; C: n=4). Statistical significance was assessed using two-way ANOVA followed by
770 Dunnett's post hoc test for multiple groups (B) or ordinary one-way ANOVA followed by Sidak's
771 post hoc test for multiple groups (C). ** $p<0.01$, *** $p<0.001$, **** $p<0.0001$.

772

773

774 *Supplemental Figure 7: Loss of mitochondrial membrane potential is independent of type-I IFN*
775 *signaling*

776 Quantification of mitochondrial membrane potential (TMRE) in HepG2 cells infected with mock
777 or YFV-17D (MOI 0.1) treated with **A** MnTBAP or **B** siMAVS to inhibit type-I IFN signaling.
778 Values represent the mean ± SD (n=3). Statistical significance was assessed using two-way
779 ANOVA followed by Tukey's post hoc test for multiple groups. ** $p<0.01$, *** $p<0.001$, ****
780 $p<0.0001$.
781
782 *Supplemental Figure 8: Peroxynitrite appears to be the main source of ROS in YFV-17D infection.*
783 **A** Quantification of peroxynitrite staining in mock, YFV-17D (MOI 0.1), and DENV2 (MOI 1)
784 infected HepG2 cells at 24hpi, 48hpi, and 72hpi using flow cytometry. **B** Flow cytometric
785 quantification of peroxynitrite staining in mock, YFV-17D, and DENV2 infected HepG2 cells
786 treated with MnTBAP or a vehicle control for 48 hours. **C and D** Growth curve quantifying the
787 viral titer and ELISA quantification of IFNβ secreted by HepG2 cells infected with **C.** YFV-17D
788 or **D** DENV2 and treated with L-NAME [5mM] at 0hpi. **E** Schematic showing the proposed
789 mechanism by which both MnTBAP and L-NAME inhibit peroxynititre formation therby blocking
790 type-I IFN production. Values represent the mean ± SD (n=3). Statistical significance was assessed
791 using two-way ANOVA followed by Dunnett's multiple comparisons test (A), ordinary one-way
792 ANOVA followed by Tukey's multiple comparisons test (B), or two-way ANOVA followed by
793 Sidak's multiple comparisons test (C, D). **** $p<0.0001$.
794
795 *Supplemental Figure 9 :MnTBAP treatment ameliorates effects of YFV-17D infection.*
796 **A** Heatmap comparing the expression of oxidative stress genes in mock and YFV-17D (MOI 0.1)
797 infected human DCs treated with and without MnTBAP.
798

799

800

801

802 **References**

803

804 1. Pierson, T.C. and M.S. Diamond, *The continued threat of emerging flaviviruses.* Nat
805 Microbiol, 2020. **5**(6): p. 796-812.
806 2. Koprowski, H. and M.B.A. Oldstone, *Microbe hunters, then and now*. 1996, Bloomington,
807 Ill.: Medi-Ed Press. 456 p.
808 3. White, C.R., *Yellow fever; history of the disease in the eighteenth and nineteenth*
809 *century.* J Kans Med Soc, 1959. **60**(8): p. 298-302 passim.
810 4. Patterson, K.D., *Yellow fever epidemics and mortality in the United States, 1693-1905.*
811 Soc Sci Med, 1992. **34**(8): p. 855-65.
812 5. Clements, A.N. and R.E. Harbach, *History of the discovery of the mode of transmission of*
813 *yellow fever virus.* J Vector Ecol, 2017. **42**(2): p. 208-222.
814 6. Theiler, M. and H.H. Smith, *The effect of prolonged cultivation in vitro upon the*
815 *pathogenicity of yellow fever virus.* Journal of Experimental Medicine, 1937. **65**(6): p.
816 767-786.
817 7. Theiler, M. and H.H. Smith, *The use of yellow fever virus modified by in vitro cultivation*
818 *for human immunization.* Journal of Experimental Medicine, 1937. **65**(6): p. 787-800.
819 8. Monath, T.P. and P.F. Vasconcelos, *Yellow fever.* J Clin Virol, 2015. **64**: p. 160-73.
820 9. Pulendran, B., *Learning immunology from the yellow fever vaccine: innate immunity to*
821 *systems vaccinology.* Nat Rev Immunol, 2009. **9**(10): p. 741-7.
822 10. Barrett, A.D. and D.E. Teuwen, *Yellow fever vaccine - how does it work and why do rare*
823 *cases of serious adverse events take place?* Curr Opin Immunol, 2009. **21**(3): p. 308-13.
824 11. Gaucher, D., et al., *Yellow fever vaccine induces integrated multilineage and*
825 *polyfunctional immune responses.* J Exp Med, 2008. **205**(13): p. 3119-31.
826 12. Akondy, R.S., et al., *Initial viral load determines the magnitude of the human CD8 T cell*
827 *response to yellow fever vaccination.* Proc Natl Acad Sci U S A, 2015. **112**(10): p. 3050-5.
828 13. Pulendran, B., *Variegation of the immune response with dendritic cells and pathogen*
829 *recognition receptors.* J Immunol, 2005. **174**(5): p. 2457-65.
830 14. Steinman, R.M. and J. Banchereau, *Taking dendritic cells into medicine.* Nature, 2007.
831 **449**(7161): p. 419-26.
832 15. Takeuchi, O. and S. Akira, *Innate immunity to virus infection.* Immunol Rev, 2009. **227**(1):
833 p. 75-86.
834 16. Douam, F., et al., *Type III Interferon-Mediated Signaling Is Critical for Controlling Live*
835 *Attenuated Yellow Fever Virus Infection In Vivo.* mBio, 2017. **8**(4).
836 17. Lam, L.K.M., et al., *Gamma-interferon exerts a critical early restriction on replication and*
837 *dissemination of yellow fever virus vaccine strain 17D-204.* NPJ Vaccines, 2018. **3**: p. 5.

838 18. Querec, T., et al., *Yellow fever vaccine YF-17D activates multiple dendritic cell subsets via*
839 *TLR2, 7, 8, and 9 to stimulate polyvalent immunity.* J Exp Med, 2006. **203**(2): p. 413-24.
840 19. Douam, F. and A. Ploss, *Yellow Fever Virus: Knowledge Gaps Impeding the Fight Against*
841 *an Old Foe.* Trends Microbiol, 2018. **26**(11): p. 913-928.
842 20. Bastard, P., et al., *Auto-antibodies to type I IFNs can underlie adverse reactions to yellow*
843 *fever live attenuated vaccine.* J Exp Med, 2021. **218**(4).
844 21. Hernandez, N., et al., *Inherited IFNAR1 deficiency in otherwise healthy patients with*
845 *adverse reaction to measles and yellow fever live vaccines.* J Exp Med, 2019. **216**(9): p.
846 2057-2070.
847 22. Suthar, M.S., et al., *A systems biology approach reveals that tissue tropism to West Nile*
848 *virus is regulated by antiviral genes and innate immune cellular processes.* PLoS Pathog,
849 2013. **9**(2): p. e1003168.
850 23. Rehwinkel, J. and M.U. Gack, *RIG-I-like receptors: their regulation and roles in RNA*
851 *sensing.* Nat Rev Immunol, 2020. **20**(9): p. 537-551.
852 24. Chatel-Chaix, L., et al., *Dengue Virus Perturbs Mitochondrial Morphodynamics to*
853 *Dampen Innate Immune Responses.* Cell Host Microbe, 2016. **20**(3): p. 342-356.
854 25. Aguirre, S., et al., *Dengue virus NS2B protein targets cGAS for degradation and prevents*
855 *mitochondrial DNA sensing during infection.* Nat Microbiol, 2017. **2**: p. 17037.
856 26. Aguirre, S., et al., *DENV inhibits type I IFN production in infected cells by cleaving human*
857 *STING.* PLoS Pathog, 2012. **8**(10): p. e1002934.
858 27. Yu, C.Y., et al., *Dengue virus targets the adaptor protein MITA to subvert host innate*
859 *immunity.* PLoS Pathog, 2012. **8**(6): p. e1002780.
860 28. Chan, K.R., et al., *Metabolic perturbations and cellular stress underpin susceptibility to*
861 *symptomatic live-attenuated yellow fever infection.* Nat Med, 2019. **25**(8): p. 1218-1224.
862 29. Querec, T.D., et al., *Systems biology approach predicts immunogenicity of the yellow*
863 *fever vaccine in humans.* Nat Immunol, 2009. **10**(1): p. 116-125.
864 30. Fernandez-Garcia, M.D., et al., *Vaccine and Wild-Type Strains of Yellow Fever Virus*
865 *Engage Distinct Entry Mechanisms and Differentially Stimulate Antiviral Immune*
866 *Responses.* mBio, 2016. **7**(1): p. e01956-15.
867 31. Sun, B., et al., *Dengue virus activates cGAS through the release of mitochondrial DNA.* Sci
868 Rep, 2017. **7**(1): p. 3594.
869 32. Castanier, C., et al., *Mitochondrial dynamics regulate the RIG-I-like receptor antiviral*
870 *pathway.* EMBO Rep, 2010. **11**(2): p. 133-8.
871 33. Onoguchi, K., et al., *Virus-infection or 5'ppp-RNA activates antiviral signal through*
872 *redistribution of IPS-1 mediated by MFN1.* PLoS Pathog, 2010. **6**(7): p. e1001012.
873 34. Plitzko, B. and S. Loesgen, *Measurement of Oxygen Consumption Rate (OCR) and*
874 *Extracellular Acidification Rate (ECAR) in Culture Cells for Assessment of the Energy*
875 *Metabolism.* Bio Protoc, 2018. **8**(10): p. e2850.
876 35. Mills, E.L., B. Kelly, and L.A.J. O'Neill, *Mitochondria are the powerhouses of immunity.*
877 Nat Immunol, 2017. **18**(5): p. 488-498.
878 36. Muri, J. and M. Kopf, *Redox regulation of immunometabolism.* Nat Rev Immunol, 2021.
879 **21**(6): p. 363-381.
880 37. Pacher, P., J.S. Beckman, and L. Liaudet, *Nitric oxide and peroxynitrite in health and*
881 *disease.* Physiol Rev, 2007. **87**(1): p. 315-424.

882 38. Hagan, T., et al., *Transcriptional atlas of the human immune response to 13 vaccines*
883 *reveals a common predictor of vaccine-induced antibody responses.* Nat Immunol, 2022.
884 **23**(12): p. 1788-1798.
885 39. Kasturi, S.P., et al., *Programming the magnitude and persistence of antibody responses*
886 *with innate immunity.* Nature, 2011. **470**(7335): p. 543-7.
887 40. Li, S., et al., *Metabolic Phenotypes of Response to Vaccination in Humans.* Cell, 2017.
888 **169**(5): p. 862-877 e17.
889 41. Ravindran, R., et al., *Vaccine activation of the nutrient sensor GCN2 in dendritic cells*
890 *enhances antigen presentation.* Science, 2014. **343**(6168): p. 313-317.
891 42. Ponia, S.S., et al., *Mitophagy antagonism by ZIKV reveals Ajuba as a regulator of PINK1*
892 *signaling, PKR-dependent inflammation, and viral invasion of tissues.* Cell Rep, 2021.
893 **37**(4): p. 109888.
894 43. Sorouri, M., T. Chang, and D.C. Hancks, *Mitochondria and Viral Infection: Advances and*
895 *Emerging Battlefronts.* mBio, 2022. **13**(1): p. e0209621.
896 44. Khan, M., et al., *Mitochondrial dynamics and viral infections: A close nexus.* Biochim
897 Biophys Acta, 2015. **1853**(10 Pt B): p. 2822-33.
898 45. Tiku, V., M.W. Tan, and I. Dikic, *Mitochondrial Functions in Infection and Immunity.*
899 Trends Cell Biol, 2020. **30**(4): p. 263-275.
900 46. Koshiba, T., et al., *Mitochondrial membrane potential is required for MAVS-mediated*
901 *antiviral signaling.* Sci Signal, 2011. **4**(158): p. ra7.
902 47. Frierson, J.G., *The yellow fever vaccine: a history.* Yale J Biol Med, 2010. **83**(2): p. 77-85.
903 48. Tur, J., et al., *Mitofusin 2 in Macrophages Links Mitochondrial ROS Production, Cytokine*
904 *Release, Phagocytosis, Autophagy, and Bactericidal Activity.* Cell Rep, 2020. **32**(8): p.
905 108079.
906 49. Chen, S., et al., *TBK1-Mediated DRP1 Targeting Confers Nucleic Acid Sensing to*
907 *Reprogram Mitochondrial Dynamics and Physiology.* Mol Cell, 2020. **80**(5): p. 810-827
908 e7.
909 50. O'Carroll, S.M., F.D.R. Henkel, and L.A.J. O'Neill, *Metabolic regulation of type I interferon*
910 *production.* Immunol Rev, 2024. **323**(1): p. 276-287.
911 51. Everts, B., et al., *TLR-driven early glycolytic reprogramming via the kinases TBK1-*
912 *IKKvarepsilon supports the anabolic demands of dendritic cell activation.* Nat Immunol,
913 2014. **15**(4): p. 323-32.
914 52. O'Neill, L.A. and E.J. Pearce, *Immunometabolism governs dendritic cell and macrophage*
915 *function.* J Exp Med, 2016. **213**(1): p. 15-23.
916 53. Olagnier, D., et al., *Cellular oxidative stress response controls the antiviral and apoptotic*
917 *programs in dengue virus-infected dendritic cells.* PLoS Pathog, 2014. **10**(12): p.
918 e1004566.
919 54. Wang, R., et al., *Influenza M2 protein regulates MAVS-mediated signaling pathway*
920 *through interacting with MAVS and increasing ROS production.* Autophagy, 2019. **15**(7):
921 p. 1163-1181.
922 55. Buskiewicz, I.A., et al., *Reactive oxygen species induce virus-independent MAVS*
923 *oligomerization in systemic lupus erythematosus.* Sci Signal, 2016. **9**(456): p. ra115.
924 56. Nobre, L., et al., *Modulation of Innate Immune Signalling by Lipid-Mediated MAVS*
925 *Transmembrane Domain Oligomerization.* PLoS One, 2015. **10**(8): p. e0136883.

926 57. Thannickal, V.J. and B.L. Fanburg, *Reactive oxygen species in cell signaling.* Am J Physiol
927 Lung Cell Mol Physiol, 2000. **279**(6): p. L1005-28.
928 58. Zhang, H., et al., *Transmembrane nitration of hydrophobic tyrosyl peptides. Localization,*
929 *characterization, mechanism of nitration, and biological implications.* J Biol Chem, 2003.
930 **278**(11): p. 8969-78.
931 59. Greenacre, S.A. and H. Ischiropoulos, *Tyrosine nitration: localisation, quantification,*
932 *consequences for protein function and signal transduction.* Free Radic Res, 2001. **34**(6):
933 p. 541-81.
934 60. Zhou, H.L., et al., *An enzyme that selectively S-nitrosylates proteins to regulate insulin*
935 *signaling.* Cell, 2023. **186**(26): p. 5812-5825 e21.
936 61. Gauba, V., et al., *Loss of CD4 T-cell-dependent tolerance to proteins with modified amino*
937 *acids.* Proc Natl Acad Sci U S A, 2011. **108**(31): p. 12821-6.
938 62. Turko, I.V., et al., *Protein tyrosine nitration in the mitochondria from diabetic mouse*
939 *heart. Implications to dysfunctional mitochondria in diabetes.* J Biol Chem, 2003.
940 **278**(36): p. 33972-7.
941 63. Hahn, C.S., et al., *Comparison of the virulent Asibi strain of yellow fever virus with the*
942 *17D vaccine strain derived from it.* Proc Natl Acad Sci U S A, 1987. **84**(7): p. 2019-23.
943 64. Lee, E. and M. Lobigs, *E protein domain III determinants of yellow fever virus 17D vaccine*
944 *strain enhance binding to glycosaminoglycans, impede virus spread, and attenuate*
945 *virulence.* J Virol, 2008. **82**(12): p. 6024-33.
946 65. McCloskey, D., et al., *A pH and solvent optimized reverse-phase ion-paring-LC-MS/MS*
947 *method that leverages multiple scan-types for targeted absolute quantification of*
948 *intracellular metabolites.* Metabolomics, 2015. **11**(5): p. 1338-1350.
949 66. Groveman, B.R., et al., *A PrP EGFR signaling axis controls neural stem cell senescence*
950 *through modulating cellular energy pathways.* J Biol Chem, 2023. **299**(11): p. 105319.
951 67. Gao, Z., et al., *Development of antibody-based assays for high throughput discovery and*
952 *mechanistic study of antiviral agents against yellow fever virus.* Antiviral Res, 2020. **182**:
953 p. 104907.
954 68. Sanchez-Velazquez, R., et al., *Generation of a reporter yellow fever virus for high*
955 *throughput antiviral assays.* Antiviral Res, 2020. **183**: p. 104939.
956 69. Cheung, A.M., et al., *Characterization of Live-Attenuated Powassan Virus Vaccine*
957 *Candidates Identifies an Efficacious Prime-Boost Strategy for Mitigating Powassan Virus*
958 *Disease in a Murine Model.* Vaccines (Basel), 2023. **11**(3).
959 70. Shannon, J.G., D. Howe, and R.A. Heinzen, *Virulent Coxiella burnetii does not activate*
960 *human dendritic cells: role of lipopolysaccharide as a shielding molecule.* Proc Natl Acad
961 Sci U S A, 2005. **102**(24): p. 8722-7.
962 71. Dobin, A., et al., *STAR: ultrafast universal RNA-seq aligner.* Bioinformatics, 2013. **29**(1):
963 p. 15-21.
964 72. Li, B. and C.N. Dewey, *RSEM: accurate transcript quantification from RNA-Seq data with*
965 *or without a reference genome.* BMC Bioinformatics, 2011. **12**: p. 323.
966 73. Ritchie, M.E., et al., *limma powers differential expression analyses for RNA-sequencing*
967 *and microarray studies.* Nucleic Acids Res, 2015. **43**(7): p. e47.

968 74. Subramanian, A., et al., *Gene set enrichment analysis: a knowledge-based approach for*
969 *interpreting genome-wide expression profiles.* Proc Natl Acad Sci U S A, 2005. **102**(43): p.
970 15545-50.
971 75. Milacic, M., et al., *The Reactome Pathway Knowledgebase 2024.* Nucleic Acids Res,
972 2024. **52**(D1): p. D672-D678.
973 76. Rath, S., et al., *MitoCarta3.0: an updated mitochondrial proteome now with sub-*
974 *organelle localization and pathway annotations.* Nucleic Acids Res, 2021. **49**(D1): p.
975 D1541-D1547.
976

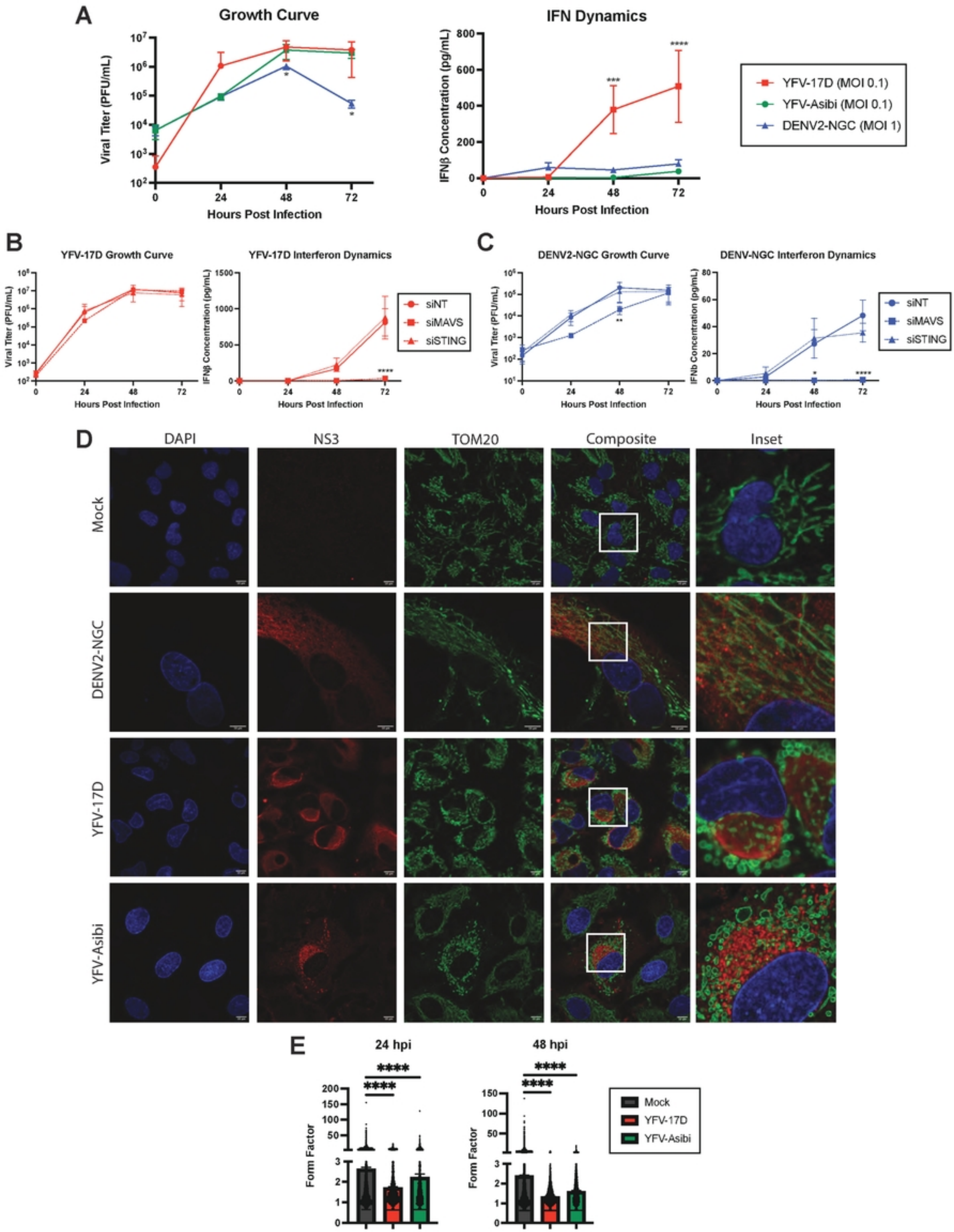
A
Growth Curve
Viral Titer (PFU/mL)
Hours Post Infection
IFN Dynamics
IFNβ Concentration (pg/mL)
Hours Post Infection
YFV-17D (MOI 0.1)
YFV-Asibi (MOI 0.1)
DENV2-NGC (MOI 1)
B
YFV-17D Growth Curve
YFV-17D Interferon Dynamics
siNT
siMAVS
siSTING
C
DENV2-NGC Growth Curve
DENV-NGC Interferon Dynamics
D
DAPI
NS3
TOM20
Composite
Inset
Mock
DENV2-NGC
YFV-17D
YFV-Asibi
E
24 hpi
48 hpi
Form Factor
Mock
YFV-17D
YFV-Asibi

Figure 1

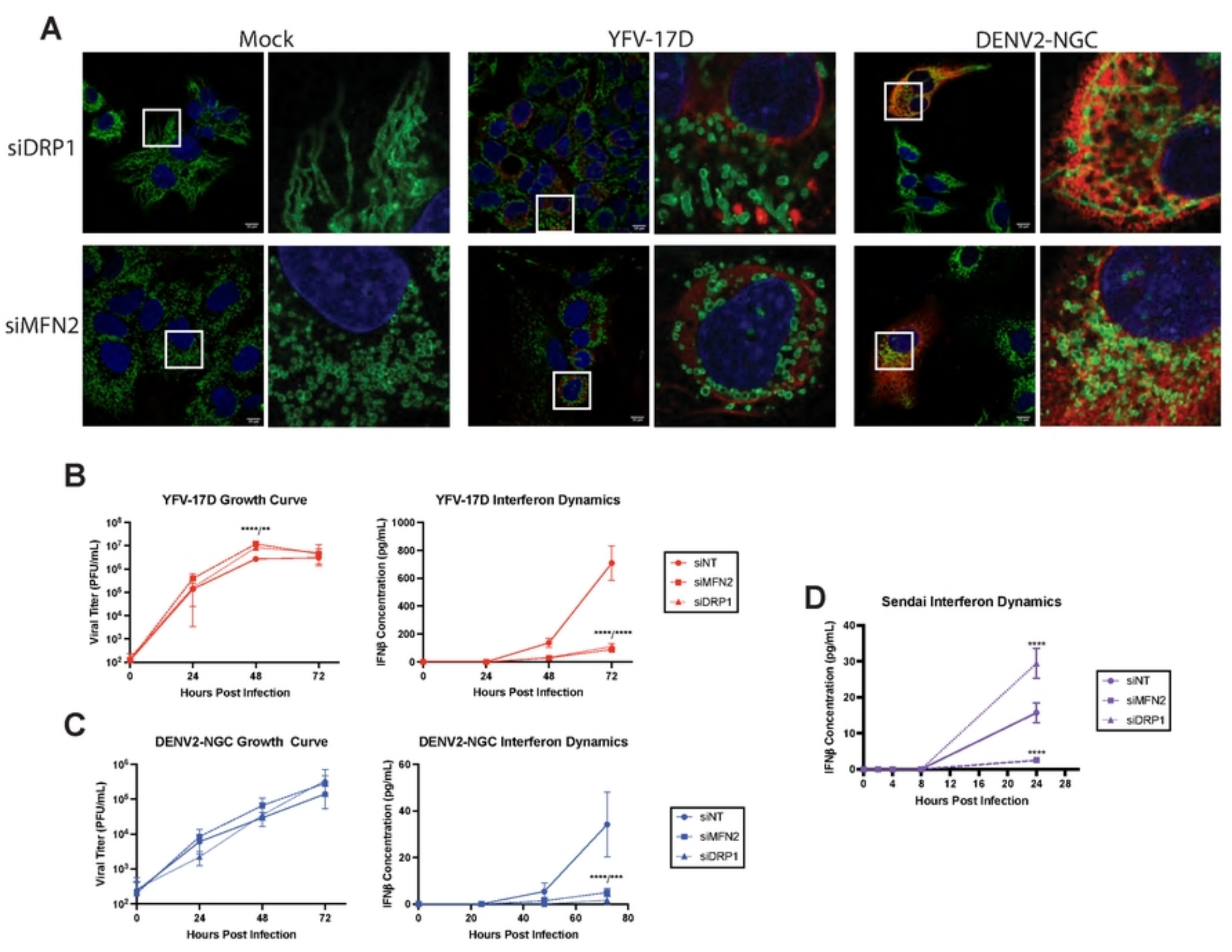
A
Mock
YFV-17D
DENV2-NGC
siDRP1
siMFN2
B
YFV-17D Growth Curve
Viral Titer (PFU/mL)
Hours Post Infection
YFV-17D Interferon Dynamics
IFNβ Concentration (pg/mL)
Hours Post Infection
siNT
siMFN2
siDRP1
C
DENV2-NGC Growth Curve
Viral Titer (PFU/mL)
Hours Post Infection
DENV2-NGC Interferon Dynamics
IFNβ Concentration (pg/mL)
Hours Post Infection
siNT
siMFN2
siDRP1
D
Sendai Interferon Dynamics
IFNβ Concentration (pg/mL)
Hours Post Infection
siNT
siMFN2
siDRP1

Figure 2

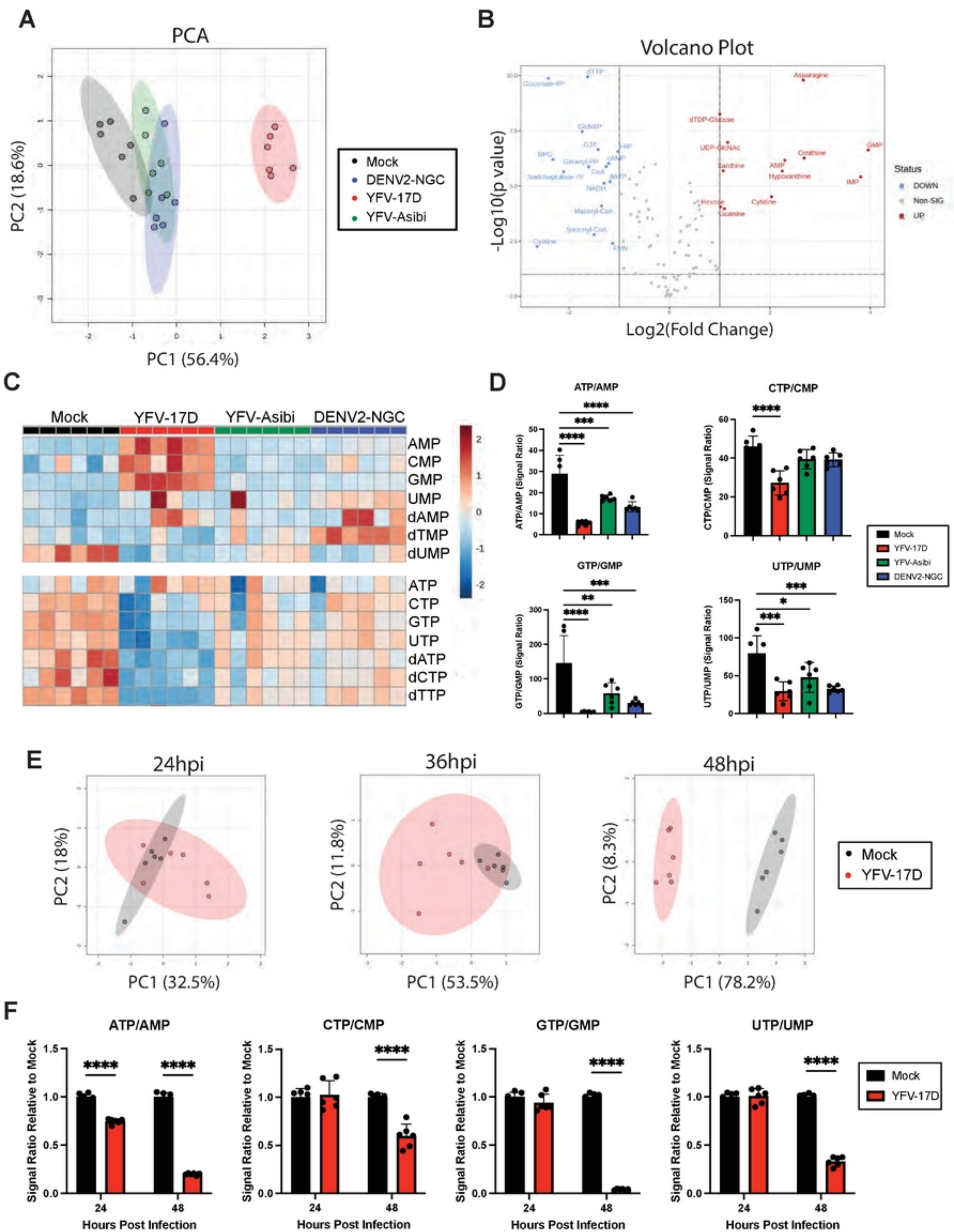
A
PCA
PC2 (18.6%)
PC1 (56.4%)
Mock
DENV2-NGC
YFV-17D
YFV-Asibi
B
Volcano Plot
-Log10(p value)
Log2(Fold Change)
Status
DOWN
Non-SIG
UP
Aspartate
dTDP-Glucose
UDP-GlcNAc
Ornithine
GMP
Xanthine
AMP
Hypoxanthine
IMP
Cytidine
Guanine
Hexose
C
Mock
YFV-17D
YFV-Asibi
DENV2-NGC
AMP
CMP
GMP
UMP
dAMP
dTMP
dUMP
ATP
CTP
GTP
UTP
dATP
dCTP
dTTP
D
ATP/AMP
CTP/CMP
GTP/GMP
UTP/UMP
ATP/AMP (Signal Ratio)
CTP/CMP (Signal Ratio)
GTP/GMP (Signal Ratio)
UTP/UMP (Signal Ratio)
Mock
YFV-17D
YFV-Asibi
DENV2-NGC
E
24hpi
36hpi
48hpi
PC2 (18%)
PC1 (32.5%)
PC2 (11.8%)
PC1 (53.5%)
PC2 (8.3%)
PC1 (78.2%)
Mock
YFV-17D
F
ATP/AMP
CTP/CMP
GTP/GMP
UTP/UMP
Signal Ratio Relative to Mock
Hours Post Infection
Mock
YFV-17D

Figure 3

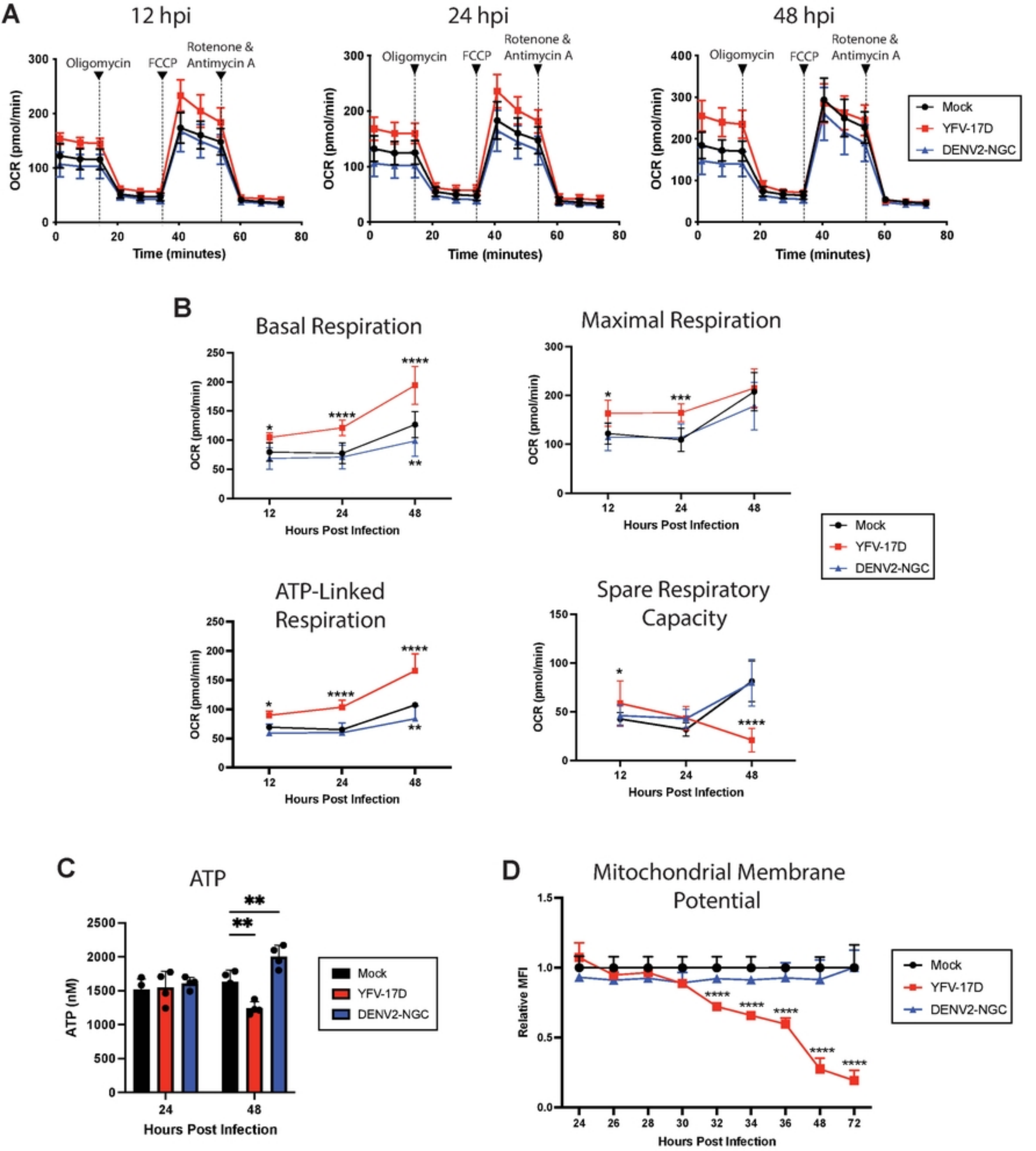
A
12 hpi
24 hpi
48 hpi
Oligomycin
FCCP
Rotenone & Antimycin A
OCR (pmol/min)
Time (minutes)
Mock
YFV-17D
DENV2-NGC
B
Basal Respiration
Maximal Respiration
ATP-Linked Respiration
Spare Respiratory Capacity
Hours Post Infection
C
ATP
ATP (nM)
D
Mitochondrial Membrane Potential
Relative MFI

Figure 4

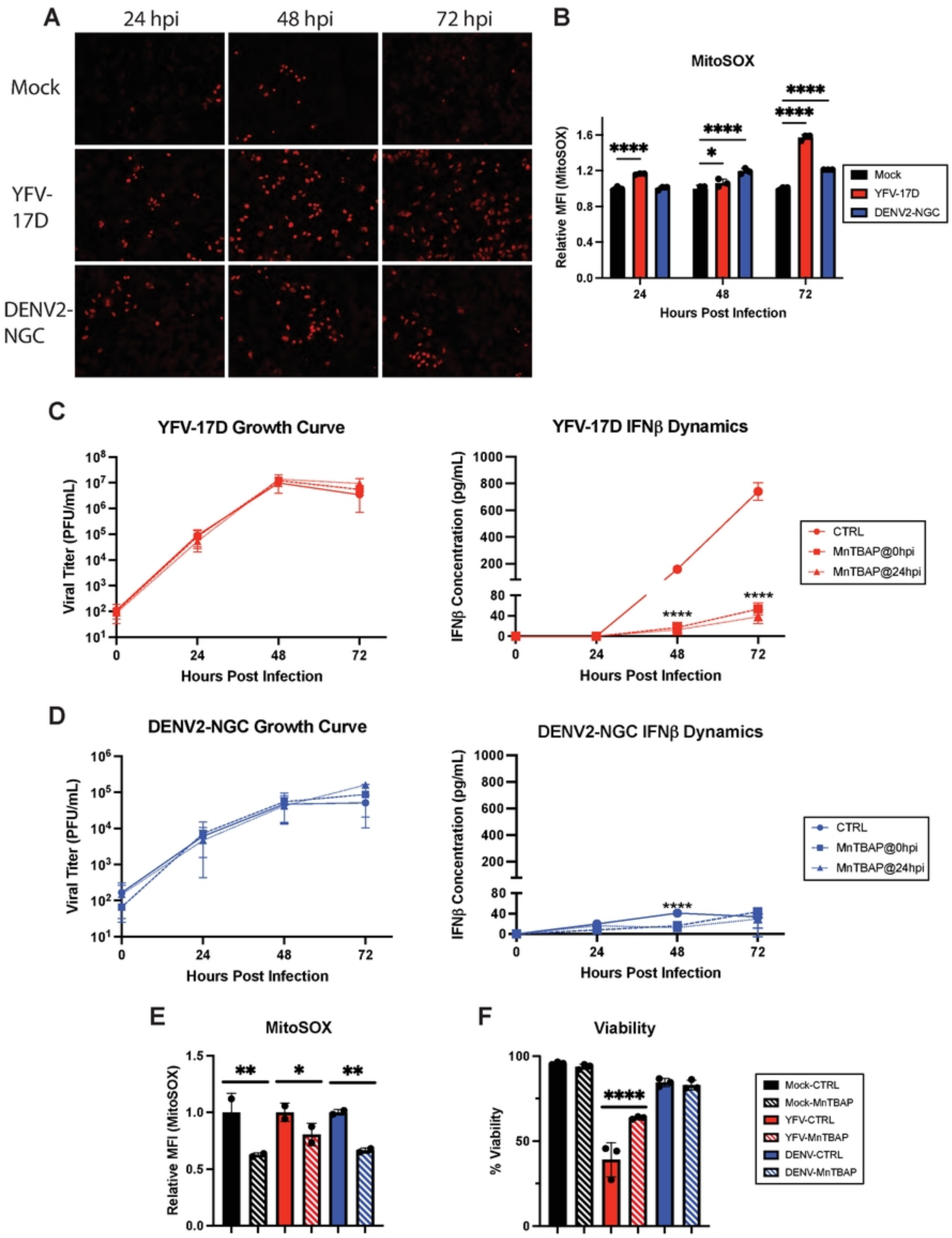
A
24 hpi
48 hpi
72 hpi
Mock
YFV-17D
DENV2-NGC
B
MitoSOX
Relative MFI (MitoSOX)
Hours Post Infection
Mock
YFV-17D
DENV2-NGC
C
YFV-17D Growth Curve
Viral Titer (PFU/mL)
Hours Post Infection
YFV-17D IFNβ Dynamics
IFNβ Concentration (pg/mL)
Hours Post Infection
CTRL
MnTBAP@0hpi
MnTBAP@24hpi
D
DENV2-NGC Growth Curve
Viral Titer (PFU/mL)
Hours Post Infection
DENV2-NGC IFNβ Dynamics
IFNβ Concentration (pg/mL)
Hours Post Infection
CTRL
MnTBAP@0hpi
MnTBAP@24hpi
E
MitoSOX
Relative MFI (MitoSOX)
F
Viability
% Viability
Mock-CTRL
Mock-MnTBAP
YFV-CTRL
YFV-MnTBAP
DENV-CTRL
DENV-MnTBAP

Figure 5

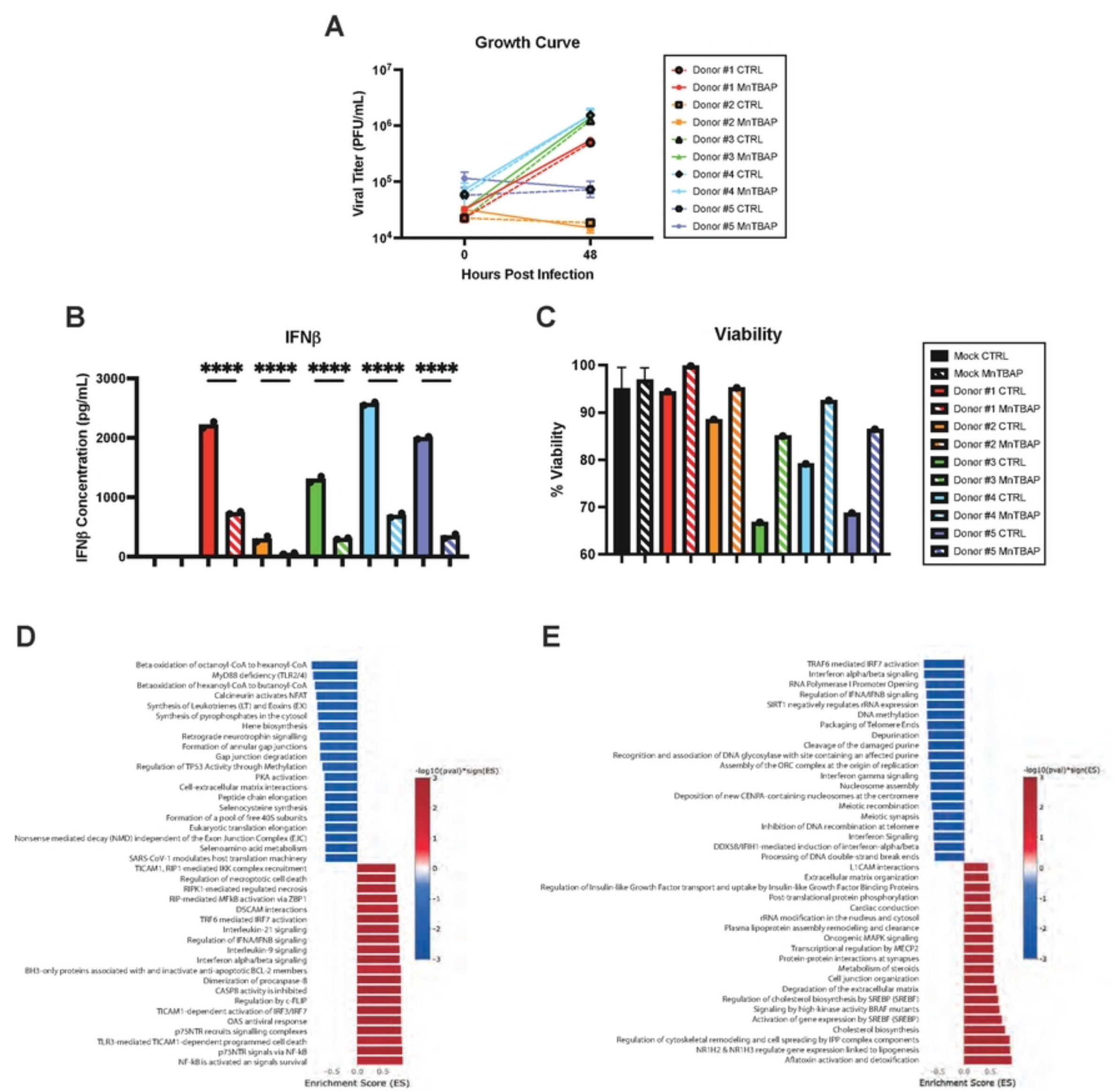
A
Growth Curve
Viral Titer (PFU/mL)
Hours Post Infection
Donor #1 CTRL
Donor #1 MnTBAP
Donor #2 CTRL
Donor #2 MnTBAP
Donor #3 CTRL
Donor #3 MnTBAP
Donor #4 CTRL
Donor #4 MnTBAP
Donor #5 CTRL
Donor #5 MnTBAP
B
IFNβ
IFNβ Concentration (pg/mL)
C
Viability
% Viability
Mock CTRL
Mock MnTBAP
D
Beta oxidation of octanoyl-CoA to hexanoyl-CoA
MyD88 deficiency (TLR2/4)
Betaoxidation of hexanoyl-CoA to butanoyl-CoA
Calcineurin activates NFAT
Synthesis of Leukotrienes (LT) and Eoxins (EX)
Synthesis of pyrophosphates in the cytosol
Heme biosynthesis
Retrograde neurotrophin signalling
Formation of annular gap junctions
Gap junction degradation
Regulation of TP53 Activity through Methylation
PKA activation
Cell-extracellular matrix interactions
Peptide chain elongation
Selenocysteine synthesis
Formation of a pool of free 40S subunits
Eukaryotic translation elongation
Nonsense mediated decay (NMD) independent of the Exon Junction Complex (EJC)
Selenoamino acid metabolism
SARS-CoV-1 modulates host translation machinery
TICAM1, RIP1-mediated IKK complex recruitment
Regulation of necroptotic cell death
RIPK1-mediated regulated necrosis
RIP-mediated MFKB activation via ZBP1
DSCAM interactions
TRF6 mediated IRF7 activation
Interleukin-21 signalling
Regulation of IFNA/IFNB signaling
Interleukin-9 signaling
Interferon alpha/beta signaling
BH3-only proteins associated with and inactivate anti-apoptotic BCL-2 members
Dimerization of procaspase-8
CASP8 activity is inhibited
Regulation by c-FLIP
TICAM1-dependent activation of IRF3/IRF7
OAS antiviral response
p75NTR recruits signalling complexes
TLR3-mediated TICAM1-dependent programmed cell death
p75NTR signals via NF-kB
NF-kB is activated an signals survival
-log10(pval)*sign(ES)
Enrichment Score (ES)
E
TRAF6 mediated IRF7 activation
Interferon alpha/beta signaling
RNA Polymerase I Promoter Opening
Regulation of IFNA/IFNB signaling
SIRT1 negatively regulates rRNA expression
DNA methylation
Packaging of Telomere Ends
Depurination
Cleavage of the damaged purine
Recognition and association of DNA glycosylase with site containing an affected purine
Assembly of the ORC complex at the origin of replication
Interferon gamma signaling
Nucleosome assembly
Deposition of new CENPA-containing nucleosomes at the centromere
Meiotic recombination
Meiotic synapsis
Inhibition of DNA recombination at telomere
Interferon Signaling
DDX58/IFIH1-mediated induction of interferon-alpha/beta
Processing of DNA double-strand break ends
L1CAM interactions
Extracellular matrix organization
Regulation of Insulin-like Growth Factor transport and uptake by Insulin-like Growth Factor Binding Proteins
Post-translational protein phosphorylation
Cardiac conduction
rRNA modification in the nucleus and cytosol
Plasma lipoprotein assembly remodeling and clearance
Oncogenic MAPK signaling
Transcriptional regulation by MECP2
Protein-protein interactions at synapses
Metabolism of steroids
Cell junction organization
Degradation of the extracellular matrix
Regulation of cholesterol biosynthesis by SREBP (SREBF)
Signaling by high-kinase activity BRAF mutants
Activation of gene expression by SREBF (SREBP)
Cholesterol biosynthesis
Regulation of cytoskeletal remodeling and cell spreading by IPP complex components
NR1H2 & NR1H3 regulate gene expression linked to lipogenesis
Aflatoxin activation and detoxification
-log10(pval)*sign(ES)
Enrichment Score (ES)

Figure 6